CORNICHON HOMOLOG 5-dependent ER export of membrane cargoes in phosphate-starved *Arabidopsis* root as revealed by membrane proteomic analysis

Tzu-Yin Liu,[1,2,3†*] Ming-Hsuan Tsai,[1†] Jhih-Yi Wang,[1†] Hui-Fang Lung,[1] Hong-Xuan Chow,[1] Chang-Yi Chiu,[1] Chiao-An Lu[3]

[1]Institute of Bioinformatics and Structural Biology, College of Life Sciences and Medicine, National Tsing Hua University, Hsinchu 30013, Taiwan.
[2]Department of Life Science, College of Life Sciences and Medicine, National Tsing Hua University, Hsinchu 30013, Taiwan.
[3]Interdisciplinary Program of Life Science and Medicine, College of Life Sciences and Medicine, National Tsing Hua University, Hsinchu 30013, Taiwan.

[*]Correspondence: Tzu-Yin Liu, tzliu@life.nthu.edu.tw
Institute of Bioinformatics and Structural Biology, College of Life Sciences and Medicine, National Tsing Hua University, Hsinchu 30013, Taiwan
Tel: +886 3 574-2096; Fax: +886 3 571-5934

[†]These authors have contributed equally to this work.
Running title: Membrane proteomics of Pi-starved *cnih5* root

The author responsible for distribution of materials integral to the findings presented in this article in accordance with the policy described in the Instructions for Authors (https://academic.oup.com/plphys/pages/General-Instructions) is: Tzu-Yin Liu (tzliu@life.nthu.edu.tw).

Key words: CORNICHON HOMOLOG, ER cargo receptor, phosphate starvation, phosphate transporter, 4-hexylphenylazosulfonate (Azo)

Abstract

Developing plants with tolerance to low phosphate (Pi) is of interest to reducing the reliance on fertilizers and thus achieving agricultural sustainability. One strategy is to enhance the endoplasmic reticulum (ER) export of cargoes associated with Pi starvation and their trafficking to final destinations. However, the mechanisms underlying this process are underexplored. We recently discovered that the *Arabidopsis thaliana CORNICHON HOMOLOG 5* (*AtCNIH5*) encodes a Pi deficiency-induced ER cargo receptor regulating Pi homeostasis. To find potential membrane cargoes of *At*CNIH5, we applied the UV-cleavable 4-hexylphenylazosulfonate (Azo)-solubilized microsomal protein extraction for iTRAQ-based proteomic analysis. We identified 4,317 proteins in Pi-limited *Arabidopsis* roots, with 372 upregulated and 106 downregulated in *cnih5*. Besides PHOSPHATE TRANSPORTER 1 proteins (PHT1s), downregulation of enzymes catalyzing the biosynthesis of very long-chain fatty acids and their derivative extracellular aliphatic compounds and nucleotide sugar for cell walls is over-represented. Using the yeast split-ubiquitin and the *in-planta* tripartite split-GFP assays, we verified the interaction of *At*CNIH5 with the downregulated transporters in *cnih5*, including *At*PHT1s, *At*OCT1, *At*URGT6, *At*DTX21, and *At*DTX35. Furthermore, *At*CNIH5 increases in the root of the Pi overaccumulator *pho2*, and its C-terminal acidic residue is not required for the interaction with *At*PHT1;1, implying that *At*CNIH5 employs a distinct selection mechanism for *At*PHT1;1. Importantly, increasing *in-situ At*CNIH5 expression/activity boosts plant growth under Pi repletion and limitation. We propose *At*CNIH5 as a low Pi-responsive hub that controls the ER export of specific membrane cargoes, thus providing a potential engineering strategy to improve plant fitness under suboptimal Pi supply.

Introduction

Phosphorus (P) is an essential macronutrient for plant growth and development (Poirier and Bucher, 2002; Poirier et al., 2022). Due to the low concentration of inorganic phosphate (Pi) in the soil—the primary form of P accessible to plants, applying Pi fertilizer has become a common practice to improve crop productivity. However, the poor mobility of Pi prevents most of the applied Pi fertilizer from acquisition, leaving P leaking into the aquatic ecosystem. Developing plants with increased Pi uptake and high-use efficiency is therefore critical to minimizing the usage of Pi fertilizer, thus reducing environmental pollution and achieving agricultural sustainability.

To adapt to the low Pi bioavailability, plants have many strategies to enhance external Pi acquisition and internal Pi remobilization, which involve different Pi transporters at distinct subcellular compartments. *PHOSPHATE TRANSPORTER 1* (*PHT1*) genes encode the plasma membrane (PM)-localized Pi transporters that are responsible for the uptake and the intercellular translocation of Pi. Even though Pi deprivation upregulates most *PHT1* genes at the transcript level, the biosynthesis, secretion, and recycling rate of PHT1 proteins (PHT1s) also determine their abundance at the PM (Nussaume et al., 2011). Multiple post-translational mechanisms have been elucidated to regulate the protein expression and the PM localization of PHT1s. The plant-specific SEC12-related PHOSPHATE TRANSPORTER TRAFFIC FACILITATOR1 (PHF1) contributes to the accumulation of PHT1s at the PM by assisting the PHT1s transit through the endoplasmic reticulum (ER) (González et al., 2005; Bayle et al., 2011; Chen et al., 2015). The rice casein kinase II (CK2) diminishes the interaction between *Os*PT8 and *Os*PHF1 by phosphorylating *Os*PT8, resulting in the ER retention of *Os*PTs (Chen et al., 2015). On the contrary, the protein phosphatase type 2C *Os*PP95 acts antagonistically with *Os*CK2 (Yang et al., 2020). In addition, under Pi sufficiency, the ubiquitin-conjugating E2 enzyme UBC24/PHOSPHATE2 (PHO2) at the ER or post-ER compartments mediates the ubiquitination of the endomembrane-associated *At*PHT1s followed by the vacuolar degradation (Huang et al., 2013). By contrast, the PM-localized ubiquitin E3 ligase NITROGEN LIMITATION ADAPTATION (NLA) participates in the endocytosis of *At*PHT1s (Lin et al., 2013; Park et al., 2014).

Incorporating diverse proteins into the coat protein complex II (COPII) vesicles or carriers at ER exit sites (ERES) requires the interaction of the COPII component Sec24

with cargoes and cargo receptors (Pagant et al., 2015). In particular, the eukaryotic conserved ER cargo receptor CORNICHON HOMOLOG proteins (CNIHs) assist the ER-to-Golgi transport of membrane proteins (Powers and Barlowe, 1998; Harmel et al., 2012). The first identified *Drosophila* CORNICHON (Cni) was shown to recruit the epidermal growth factor (EGF)-like ligand Gurken into COPII vesicles (Bökel et al., 2006). Without Cni, the ER export and secretion of Gurken are disrupted (Bökel et al., 2006). Loss of the fungal CNIH/Erv14 comprised the targeting of several transporters destined for the late secretory compartments, thus misregulating numerous cellular functions (Powers and Barlowe, 1998; Nakanishi et al., 2007; Pagant et al., 2015; Zimmermannová et al., 2019; Zheng et al., 2023). Similarly, the plant CNIHs act as the ER cargo receptors for various ion and metabolite transporters (Rosas-Santiago et al., 2015; Wudick et al., 2018; Wei et al., 2023; Yáñez-Domínguez et al., 2023).

Our recent side-by-side study uncovered that the *Arabidopsis thaliana CORNICHON HOMOLOG 5* (*AtCNIH5*) is a Pi starvation-induced (PSi) gene and preferentially expressed in the outer layers of the root above the apical meristem (Chiu et al., 2024). The fluorescent protein tagged-*At*PHT1;1 was partially retained intracellularly in the root epidermis within the transition/elongation zones and in the root hair of the Pi-limited *cnih5* (Chiu et al., 2024). The fluorescence intensities of *At*PHT1;1 fusion proteins also diminished at the PM of the root cells mentioned above in the Pi-limited *cnih5* relative to the WT control (Chiu et al., 2024). In agreement with the role of *At*CNIH5 in the ER export of *At*PHT1s at ERES, the *cnih5* mutant exhibited a lower abundance of *At*PHT1s in the root microsomal fractions, with reduced shoot Pi levels under Pi sufficiency and decreased Pi uptake under Pi deficiency (Chiu et al., 2024). Additional phenotypes, such as shorter root hair length and increased root hair and lateral root densities, were also observed for *cnih5* under Pi deficiency (Chiu et al., 2024). Considering that *At*CNIH5 may serve as a cargo receptor for a broader range of membrane proteins and inefficient ER export of cargoes in *cnih5* can cause their intracellular retention and eventually degradation due to the protein quality control, we inferred that the pleiotropy of *cnih5* is likely consequences of mistargeting and/or downregulation of cognate cargoes of *At*CNIH5.

To identify potential membrane cargoes of *At*CNIH5 associated with Pi starvation responses, we employed isobaric tags for relative and absolute quantification (iTRAQ)-

based quantitative membrane proteomics. Because membrane proteins are highly hydrophobic and have low abundance, isolation of microsomal proteins (MPs) enriched for PM, ER, Golgi, vacuolar membranes, and endosomal vesicles is challenging (Wang and Liang, 2012). Conventionally, MPs are solubilized with sodium dodecyl sulfate (SDS) or other anionic detergents. However, SDS impacts the liquid chromatography-tandem mass spectrometry (LC-MS/MS) performance, and the removal step of SDS before MS analysis leads to an inevitable loss of MPs (Wang and Liang, 2012). A study using the rice leaf as a model system demonstrated that the microcentrifugation-based microsomal protein extraction (MME) method is effective for the downstream label-free quantitative proteome analysis, requiring neither a large amount of plant material nor a step of ultracentrifugation to enrich the PM proteins (Nguyen et al., 2021). The authors also applied the UV-cleavable and MS-compatible surfactant, 4-hexylphenylazosulfonate (Azo) (Brown et al., 2019; Brown et al., 2020), to avoid protein losses by omitting the SDS detergent wash step. Their results revealed several advantages of Azo over SDS in solubilizing the MPs, including a higher number and abundance of MPs (Nguyen et al., 2021). In this study, we modified the Azo-solubilized MME method and isolated the root MPs from Pi-limited *Arabidopsis* WT and *cnih5* for iTRAQ-based proteomic analysis. We targeted our research to root MPs to reduce sample complexity, thus increasing the possibility of identifying functionally relevant protein changes in *cnih5*. In addition, the membrane proteome analysis of Pi-limited roots is valuable in gaining insight into the physiological role of *At*CNIH5. It also provides the first database of the membrane proteome for Pi-limited root biology research (Zhou et al., 2022).

With this approach, we identified 4,317 proteins in the Pi-limited WT and *cnih5* roots, in which 1231 proteins (28.5%) have at least one transmembrane helix. Of the differentially expressed proteins in *cnih5*, 372 and 106 proteins are upregulated and downregulated by a 1.25-fold change, respectively, including the downregulation of *At*PHT1;1–1;5, corroborating our recent finding that *At*PHT1s are genuine cargoes of *At*CNIH5 (Chiu et al., 2024). Consistent with the primary role of *At*CNIH5 in the ER-to-Golgi transport of membrane cargoes, the enrichment analyses of Gene Ontology (GO) terms and Kyoto Encyclopedia of Genes and Genomes (KEGG) pathways suggested a close association of downregulated proteins with protein export and localization. We also found that enzymes involved in the biosynthesis of nucleotide sugar for cell walls, very

long-chain fatty acids (VLCFAs), and their derivative extracellular aliphatic compounds, such as suberin, were downregulated in the Pi-limited *cnih5* roots.

We used the yeast split-ubiquitin system (SUS) and the *in-planta* tripartite split-GFP assay to confirm the interaction of the potential membrane cargoes with *At*CNIH5, including *At*PHT1s and several transporters. In line with the notion that *At*CNIH5 mediates the ER export of *At*PHT1s, *At*CNIH5 increases in the root of Pi overaccumulator *pho2* under ample Pi supply, likely as a result of accommodating the increased demand for ER export of *At*PHT1s. We also generated a series of C-terminally truncated forms of *At*CNIH5 to find out which motif of *At*CNIH5 interacts with *At*PHT1;1 and showed that *At*CNIH5 1–26, containing the TMD1 alone, is sufficient for interacting with *At*PHT1;1. Instead, the C-terminal acidic residue, aspartic acid, is not required for the interaction with *At*PHT1;1. Therefore, unlike the fungal and rice CNIHs interacting with their cognate cargoes through the C-terminal acidic motif (Rosas-Santiago et al., 2017), *At*CNIH5 employs a distinct mechanism to select *At*PHT1;1 as its membrane cargo. Importantly, introducing the *At*CNIH5 genomic-GFP translation fusion to complement the *cnih5* mutant boosted plant growth under suboptimal Pi supply, revealing that *At*CNIH5 acts as a hub that facilitate the ER export of specific membrane cargoes associated with Pi starvation to improve plant fitness.

Results

Azo-solubilized microcentrifugation-based microsomal protein extraction (MME) of *Arabidopsis* roots

Because the application of Azo promoted fast and reproducible tryptic digestion for quantitative proteomics (Brown et al., 2020), we replaced the MS-incompatible surfactant SDS with Azo and established an efficient workflow of MPs extraction for quantitative proteomic analysis of *Arabidopsis* roots (**Supplementary Fig. S1**). To ensure that the Azo wash step can be skipped prior to MS analysis, we tested the time-course effect of UV irradiation on Azo breakdown (Brown et al., 2019). Within 40 min of UV illumination, 1% Azo in 100 mM triethylammonium bicarbonate (TEABC) almost wholly degraded (**Supplementary Fig. S2**). After tryptic digestion and Azo degradation, small aliquots of four samples—two biological replicates each for WT and *cnih5*, were pre-analyzed in a single one-dimensional (1D)–LC-MS/MS run. We used multiple

marker abundance profiling (MMAP) (Hooper et al., 2016) to estimate the relative organelle abundance in the samples of MPs. The results suggested that the modified Azo-solubilized MME method greatly removed proteins targeted to the plastid, nucleus, and extracellular space while enriching proteins targeted to the mitochondria, ER, Golgi, PM, and vacuole (**Supplementary Fig. S3**). To further evaluate the modified Azo-solubilized MME method, we also examined by immunoblot the expression of well-established root MPs, including the ER-resident *At*PHF1, the Golgi-localized *At*PHO1 (Arpat et al., 2012; Liu et al., 2012), and the PM-targeted *At*NRT2.1 (Chopin et al., 2007). As previously reported (Liu et al., 2012; Huang et al., 2013), *At*PHF1 and *At*PHO1 were upregulated following Pi deprivation. Interestingly, regardless of Pi availability, the protein amounts of *At*PHF1 and *At*PHO1 were more abundant in *cnih5* than in WT (**Fig. 1A**). On the other hand, *At*NRT2.1 expression declined by Pi starvation and showed no differences between WT and *cnih5* (**Fig. 1A**). Collectively, these results justified the suitability of our modified Azo-solubilized MME method for enriching root MPs.

Upregulation of *At*CNIH5 in the root of the Pi overaccumulator *pho2*

As we attempted to determine the expression of *At*CNIH5 in the root MPs, a specific polyclonal antibody against *At*CNIH5 was raised. This antibody recognized a band in the WT at ∼15 kDa that was absent in *cnih5* (**Fig. 1B**). In agreement with the finding that low Pi induces the gene expression of *AtCNIH5* (Chiu et al., 2024), the protein amount of *At*CNIH5 was also elevated in the Pi-limited root (**Fig. 1B**), indicating that *AtCNIH5* is upregulated by Pi starvation at the transcript and protein level. Of note, under Pi sufficiency, *At*CNIH5 was modestly increased in the root of the Pi overaccumulator *pho2* relative to the WT control (**Fig. 1B**). We could recapitulate the observation of increased *At*CNIH5 in *pho2* by two other different MPs extraction methods (**Fig. 1B**). These results suggested that *At*CNIH5 elevates to accommodate the increased demand for ER export of *At*PHT1s, which is substantiated by our genetic evidence that loss of *AtCNIH5* alleviates the Pi toxicity of *pho2* (Chiu et al., 2024).

Quantitative membrane proteomic analysis of MPs in *Arabidopsis cnih5* roots under Pi limitation

Next, the peptides obtained after tryptic digestion were labeled with iTRAQ reagents,

combined, and separated by two-dimensional high-performance liquid chromatography (2D–HPLC) into 24 fractions. Each fraction was diluted and trapped onto a reverse-phase column for separation, followed by Orbitrap mass spectrometry. By combining the total proteins of the four samples, we identified 32,812 peptides and 21,433 unique peptides that matched with 4,317 proteins with confidence (criteria described in Material and Method), resulting in an average sequence coverage of 17.8% (**Supplementary Table S1**). About 99.3% of the identified proteins were shared across the four samples (**Supplementary Table S1**), indicating that our proteomic data were unbiased, as nearly all proteins within the detection range could be identified. The proteins containing transmembrane helices were predicted or annotated by DeepTMHMM and UniProtKB (**Fig. 2A)** (Krogh et al., 2001; Hallgren et al., 2022; The UniProt Consortium, 2023). 1231 identified proteins (28.5%) have at least one transmembrane helix and are thus integral membrane or transmembrane (TM) proteins (**Fig. 2A**). We classified the subcellular localizations of the 4,317 identified proteins using SUBA5 (Hooper et al., 2016), showing 7.8% of the identified proteins localized to the ER, 10.1% to the Golgi, 4.4% to the vacuole, and 16.2% to the PM (**Fig. 2B**). About 37.3% (1609) and 21.2% (915) of the identified proteins represent MPs and integral MPs, respectively (**Fig. 2A**). In contrast, 19.3% of the 1231 TM proteins localized to the ER, 15.7% to the Golgi, 9.7% to the vacuole, and 31.7% to the PM (**Fig. 2C**). The general and detailed descriptions of proteomics data, including the summary of proteomic analysis, protein scores and mass, annotation, and quantification for the identified proteins, are listed in **Supplementary Table 1**. We then subjected the 4,317 identified proteins to GO enrichment analysis by ShinyGO 0.80 (Ge et al., 2019) (**Supplementary Table S1**). Only the top significant GO terms (FDR adj. p-value ≤ 0.05) (**Fig. 3A**) and the hierarchical clustering trees of GO terms (**Fig. 3B**) were shown according to the ranking of fold enrichment. In the molecular function (MF) category, the top three are nucleoside-triphosphatase activity, pyrophosphatase activity, and mRNA binding; in the biological process (BP) category, the top three are intracellular transport, protein transport, and establishment of protein localization; in the cellular component (CC) category, the top three are plant-type vacuole, cell-cell junction, and plasmodesmata.

To compare the MPs profiling between WT and *cnih5*, we defined proteins as differentially expressed when at least two ratios (fold changes) are ≥ 1.25 or ≤ 0.75,

excluding candidates with ratios of opposite trends. Accordingly, 372 and 106 proteins are upregulated and downregulated, respectively, in at least one biological replicate of *cnih5* (**Supplementary Table S2**). The upregulated proteins in the Pi-limited *cnih5* roots, likely reflecting compensation mechanisms for loss of *At*CNIH5, were subjected to GO enrichment analysis. In the MF category, the top three include copper ion binding, antioxidant activity, and oxidoreductase activity acting on the CH–OH group of donors NAD or NA (**Supplementary Fig. S4** and **Supplementary Table S2**); in the BP category, the top three are sulfur compound biosynthetic process, purine nucleotide metabolic process, and purine-containing compound metabolic process (**Supplementary Fig. S4** and **Supplementary Table S2**); in the CC category, polysomal ribosome, polysome, and cytosolic ribosome are enriched (**Supplementary Fig. S4** and **Supplementary Table S2**). The KEGG analysis identified the top three pathways (FDR adj. p-value ≤ 0.05) that pertain to ascorbate and aldarate metabolism, sulfur metabolism, and fructose and mannose metabolism (**Supplementary Fig. S5**), suggesting an association of the upregulated proteins in the Pi-limited *cnih5* roots with carbohydrate metabolic pathways that protect cells against oxidative stress. The downregulated proteins were also subjected to the enrichment analysis of GO terms and KEGG pathways (FDR adj. p-value ≤ 0.05). In the MF category, 7S RNA binding, fatty acid elongase activity, structural constituent of chromatin, and transmembrane transporter activity are the top terms (**Fig. 4** and **Supplementary Table S2**); in the BP categories, the top three are protein transport, cellular macromolecule localization, and establishment of protein localization (**Fig. 4** and **Supplementary Table S2**); in the CC categories, AP-type membrane coat adaptor complex, membrane coat, coated membrane, and cytoplasmic vesicle membrane are enriched (**Fig. 4** and **Supplementary Table S2**). The top four KEGG pathways involve fatty acid elongation, protein export, cutin, suberin, and wax biosynthesis, and biosynthesis of nucleotide sugars (**Supplementary Fig. S5**). Overall, the downregulated proteins in the Pi-limited root of *cnih5* are linked to protein export and localization, acyl-lipid metabolism, and nucleotide sugar biosynthesis.

Assuming that potential cargoes of *At*CNIH5 are downregulated integral MPs in *cnih5*, we narrowed the number of candidates to 31 (**Table 1**). This list is over-represented with three hypersensitive response-like lesion-inducing protein (HRLI)-like proteins (AT3G23175, AT3G23190, and AT4G14420), two β-ketoacyl-CoA synthases (*At*KCS2

and *At*KCS20), and two *At*PHT1 members (*At*PHT1;1 and *At*PHT1;3) (**Table 1**). Several *At*PHT1 members were downregulated in the Pi-limited root of *cnih5* versus wild-type (WT) (**Table 2**). Specifically, downregulation of *At*PHT1;2, *At*PHT1;3, or *At*PHT1;4 was found in at least one biological replicate of *cnih5* (FDR adj. *p*-value ≤ 0.05). Despite not being statistically significant, the upregulation of *At*PHF1 and the downregulation of *At*PHT1;1 and *At*PHT1;5 displayed a similar trend of change in at least two biological replicates of *cnih5*. By contrast, *At*PHT1;9 was unexpectedly upregulated in the Pi-limited root of *cnih5* (**Table 2**).

Analysis of protein–protein interaction between *At*CNIH5 and its potential membrane cargoes

Next, we selected a subset of the potential membrane cargoes (highlighted in gray in **Table 1**) to test their interaction with *At*CNIH5 based on the two criteria: (1) a TM protein located in the post-ER compartments of the secretory pathway and (2) showing at least two ratios (fold-change) ≤ 0.75 or at least one ratio ≤ 0.75 with FDR adj. *p*-value < 0.05. With the yeast SUS, the nutrient selection and LacZ *β*-galactosidase assays suggested that besides *At*PHT1;1 and *At*PHT1;4 (Chiu et al., 2024), *At*CNIH5 also interacted with *At*PHT1;2, *At*PHT1;5, *At*PHT1;7 and *At*PHT1;9 (**Fig. 5A**), suggesting that *At*CNIH5 recognizes conserved motifs among several *At*PHT1 members. We also verified the interaction of *At*CNIH5 with the PM-localized receptor-like kinase AtLRK10L-1.1 (AT1G18390), nucleotide exchange factor *At*SOS (AT1G26650), and organic cation/carnitine transporter *At*OCT1 (AT1G73220), the Golgi-localized nucleotide sugar transporters *At*URGT6 (AT1G34020) and glucuronoxylan 4-O-methyltransferase *At*GXM2 (AT4G09990), and the tonoplast (TP)-localized detoxification efflux carriers *At*DTX21 (AT1G33110) and *At*DTX35 (AT4G25640) (**Fig. 5B)**. Consistently, we obtained similar results when the expression constructs for *At*SOS, *At*OCT1 *At*URGT6, *At*DTX21, and *At*DTX35 were generated with different fusion orientations (**Supplementary Fig. S6**).

To explore other potential membrane cargoes of *At*CNIH5 that may be missing in our proteomic data, we set out in parallel to find root PSi genes encoding transporters that are co-regulated with *AtCNIH5*. We queried the RNA-seq dataset from *Arabidopsis* seedlings subjected to Pi deprivation (P0: Pi-sufficiency; P1: one day of Pi deprivation; P3: three

days of Pi deprivation) (Liu et al., 2016). Genes with expression levels less than 1 RPKM were excluded. We filtered root PSi genes that displayed an expression pattern similar to that of *AtCNIH5* based on (1) the $\log_2$ fold change (FC) ≥ 0.5 (P1/P0), (2) the $\log_2$FC ≥ 1 (P3/P0), and (3) the difference of $\log_2$FC ≥ 0.5 (P3/P0−P1/P0). Such cutoffs were applied to root PSi genes because the agriGO enrichment analysis (Tian et al., 2017) yielded a satisfactory list for further investigation, including nearly all *At*PHT1s and more than ten other genes encoding transporters (**Supplementary Table S3**). Among the list, the PM-localized *At*OCT1, potassium transporter *At*HAK5, sulfate transporter *At*SULTR1;3, and the TP-localized Pi transporter *At*VPE1 were selected for testing the interaction with *AtC*NIH5 based on tripartite split-GFP association in agro-infiltrated *N. benthamiana* leaves (Liu et al., 2018; Liu, 2021). We also included *At*SOS, *At*URGT6, *At*DTX21, and *At*DTX35 for testing but not *At*LRK10L-1.1 and *At*GXM2 due to the same membrane topology of *At*CNIH5 and *At*GXM2 and the failure to find any agrobacteria transformants carrying the *At*LRK10L-1.1 construct. The S10-tagged *At*CNIH5 (S10-*At*CNIH5) and the S11-tagged fusion protein of interest correctly reached their subcellular destinations, except that *At*SOS-S11 and *At*SULTR1;3-S11 were retained in the ER (**Fig. 6A**). Compared to the positive control *At*PHT1;1-S11 and the negative control 3xHA-S11 as recently reported (Chiu et al., 2024), S10-*At*CNIH5 also interacted with *At*OCT1-S11, *At*SOS-S11, *At*URGT6-S11, *At*DTX21-S11, and *At*DTX35-S11 *in planta*, yielding fluorescence signals as a result of GFP complementation, but failed to interact with *At*HAK5-S11, *At*SULTR1;3-S11, and *At*VPE1-S11 (**Fig. 6B**). Taken together, these results supported that our comparative proteomics successfully identified specific membrane cargoes of *At*CNIH5, including *At*PHT1s.

The C-terminal acidic residue of *At*CNIH5 is not required for the interaction with *At*PHT1;1

As several *At*PHT1 members were identified as prominent cargoes of *At*CNIH5, we were curious to find out which motif of *At*CNIH5 interacts with *At*PHT1;1. *At*CNIHs have three putative transmembrane domains (TMD), with the N terminus facing the cytosol, the C terminus facing the ER lumen, and at least four putative functional motifs (Wudick et al., 2018; Chiu et al., 2024). The putative FLN motif in the second TMD of *Sc*Erv14, known as a cargo-binding site (Pagant et al., 2015), is present in *At*CNIH2–4, denoted as

the YLC motif. The putative cytosolic IFRTL motif, located between the second and third TMD of *Sc*Erv14 and interacting with Sec24 (Powers and Barlowe, 2002), is also conserved in *At*CNIH2–4 with several residues changed, denoted as the IFNNL motif. The C-terminal acidic motif, which is only found in plants and fungi, is required for *Sc*Erv14 to assist the PM targeting of the yeast Nha1, Pdr12, and Qdr2 as well as for the rice *Os*CNIH1 to aid the Golgi targeting of *Os*HKT1;3 (Rosas-Santiago et al., 2017). Besides the cornichon motif that is well conserved among all *At*CNIHs, *At*CNIH5 has the putative YLC and IFNNL motifs with several residues changed and a shorter C-terminal putative acidic motif with one aspartic acid residue (**Supplementary Fig. S7**). We designed a series of C-terminally truncated forms of *At*CNIH5. For unknown reasons, we failed to obtain the clone expressing *At*CNIH5 1–102. Therefore, we only tested the interaction of *At*PHT1;1 with *At*CNIH5 1–26, *At*CNIH5 1–49, *At*CNIH5 1–92, and *At*CNIH5 1–132 in the yeast SUS (**Fig. 7A**). Interestingly, *At*CNIH5 1–26, which contains only the first TMD, is sufficient to interact with *At*PHT1;1. By comparison, *At*CNIH5 1–132, in which the last three amino acids are deleted, including the C-terminal aspartic acid, could still interact with *At*PHT1;1 (**Fig. 7B**), suggesting that the putative C-terminal motif of *At*CNIH5 is not required for interacting with *At*PHT1;1 and *At*CNIH5 employs a distinct mechanism to interact with *At*PHT1;1 from those utilized by the fungi and rice CNIHs for their cognate cargoes.

Increasing *in-situ At*CNIH5 expression/activity enables robust plant growth

Since the loss of *At*CNIH5 led to decreased abundance of *At*PHT1s (**Table 2**), it becomes imperative to inspect whether overexpression of *At*CNIH5 can improve plant fitness under Pi limitation. Unexpectedly, the ectopic expression of RFP-*At*CNIH5 under the cauliflower mosaic virus (CaMV) 35S promoter was shown to confer abnormal root morphology (Chiu et al., 2024). Instead, the transgenic lines expressing the genomic GFP-*AtCNIH5* fragment (*AtCNIH5pro*: GFP-*AtCNIH5*) in the *cnih5* background restored the expression of *At*PHT1;1/2/3 to the WT-like level and surprisingly grew bigger than WT and *cnih5* when Pi is repleted (Chiu et al., 2024). We then systematically examined the growth of these *cnih5* complemented lines under different Pi regimes. Under Pi sufficiency and modest Pi deficiency—three days of Pi deprivation (0 μM Pi) or eleven days of suboptimal Pi supply (50 μM Pi), the complemented *cnih5* lines exhibited higher

shoot and/or root fresh weight than the WT and *cnih5* plants (**Fig. 8**). By contrast, under severe Pi deficiency—eleven days of Pi deprivation (0 μM Pi), only one complemented line showed bigger shoot than WT (**Fig. 8**). Although we could detect the expression of GFP-*AtCNIH5* proteins in the Pi-limited root of the *cnih5* complemented lines, it is technically challenging to discern whether GFP-*AtCNIH5* proteins were more abundant than the endogenous *At*CNIH5 in WT (**Supplementary Fig. S8**). Nevertheless, the higher biomass of the *cnih5* complemented lines is likely attributed to more efficient assimilation of acquired Pi for plant growth as a result of increased expression/activity of GFP-*AtCNIH5*, accompanied by the concerted upregulation of membrane cargoes of *At*CNIH5 besides *At*PHT1s. We thus inferred that a subtle increase of *in-situ* rather than ectopic expression/activity of GFP-*AtCNIH5* suffices to activate downstream effectors of *At*CNIH5, thereby boosting plant growth.

Discussion

CNIHs are the eukaryotic conserved cargo receptors that cycle between the ER and the early Golgi to select membrane proteins into COPII vesicles. In this study, we aimed to discover potential membrane cargoes of low Pi-induced *At*CNIH5 by iTRAQ-based proteomic analysis and, in the meantime, to provide the first membrane proteome for *Arabidopsis* roots subjected to Pi deprivation (Zhou et al., 2022). In a previous study using Pi-deficient *Arabidopsis* roots for quantitative total protein profiling, membrane-associated proteins were underrepresented (Lan et al., 2012). Compared with the 209 significantly up-regulated proteins in their datasets (Pi-deficient/Pi-sufficient plants ratio of ≥ 1.29), only 61 proteins overlapped with the identified 4317 proteins of Pi-limited roots in this study (**Supplementary Table S1)**. Therefore, enriching MPs for membrane proteomics could greatly expand the inventory of identified proteins implicated in Pi starvation responses.

According to the GO enrichment analysis of the 106 downregulated proteins in the Pi-limited *cnih5* roots, most of the enriched terms in the BP category are closely associated with protein transport and localization (**Fig. 4**), which is line with the role of *At*CNIH5 in the ER-to-Golgi membrane cargo trafficking. Notably, the GO terms "AP-type membrane coat adaptor complex" in the CC category and "7S RNA binding" in the MF category were over-representative (**Fig. 4**). This can be attributed to the downregulation of proteins

involved in the Golgi-associated clathrin assembly and the signal recognition particle (SRP) subunits mediating the co-translational membrane protein targeting (**Supplementary Table 2**). We surmised that loss of *At*CNIH5 likely initiates negative feedback regulation on the post-Golgi membrane trafficking to reduce the futile coated-vesicle assembly and on the protein synthesis to avoid the toxic accumulation of *At*CNIH5-dependent cargoes in the ER.

Moreover, our comparative proteome analysis revealed that 31 integral MPs were downregulated in the Pi-limited *cnih5* roots (**Table 1**). Of them, two *At*PHT1s (*At*PHT1;1 and *At*PHT1;3), two *At*KCS (*At*KCS2 and *At*KCS20), and three *At*HRLI-like proteins are over-represented. While *AtKCS* genes encode 3-ketoacyl CoA synthases catalyzing the rate-limiting condensation step of VLCFAs biosynthesis (Evenson and Post-Beittenmiller, 1995), *AtKCS2* and *AtKCS20* are highly expressed in the root endodermis and functionally redundant in root suberin biosynthesis (Lee et al., 2009). Interestingly, two alcohol-forming fatty acyl-CoA reductases, *At*FAR3/CER4 and *At*FAR5, are also downregulated and over-represented in the KEGG pathway of cutin, suberin and wax biosynthesis (**Supplementary Fig. 6** and **Supplementary Table 2**). These results suggested that VLCFAs and their derivative extracellular aliphatic compounds are misregulated in the Pi-limited *cnih5* roots. Although *At*HRLI-like proteins have not been functionally characterized, the *N. benthamiana Nb*HRLI4 conferred salicylic acid-mediated resistance to turnip mosaic virus (TuMV) (Wu et al., 2021). Since *At*KCS and *At*HRLI-like proteins are ER-localized integral MPs, downregulation of these membrane proteins may be a secondary effect due to the impairment of *At*CNIH5.

Considering that only integral MPs at the post-ER compartments are potential cargoes of *At*CNIH5, we tested their interaction with *At*CNIH5. When expressed in the yeast heterologous expression system, *At*CNIH5 interacted not only with the two major Pi transporters for Pi uptake, *At*PHT1;1 and *At*PHT1;4 (Chiu et al., 2024), but also with *At*PHT1;2, *At*PHT1;5, *At*PHT1;7, and *At*PHT1;9 (**Fig. 5A**), supporting that *At*PHT1s are the prominent membrane cargoes of *At*CNIH5 under Pi starvation. This was not surprising because the amino acid sequences of *At*PHT1s share over 47.4% identity. It has been shown that the yeast and rice CNIHs used the C-terminal acidic motif to interact with their cognate cargoes (Rosas-Santiago et al., 2017). However, a recent study revealed that the cargo binding motif of the pumpkin *Cm*CNIH1 may reside in the N-

terminal rather than the C-terminal region (Wei et al., 2023), which was in agreement with our results for *At*CNIH5 (**Fig. 7B**).

Besides *At*PHT1s, we identified other PM-localized membrane proteins downregulated in the Pi-limited *cnih5* roots. *At*LRK10L-1.2 is involved in ABA signaling (Lim et al., 2015) and the animal Son of Sevenless (SOS) proteins encode the guanine nucleotide exchange factors acting on the Ras subfamily of small GTPases (Bowtell et al., 1992). However, the physiological role of SOS in plants remains to be studied. Like *AtCNIH5*, *AtOCT1* is also a PSi gene (**Supplementary Table S3**). The expression of *AtOCT1* is restricted to the vasculature of the root and at sites of lateral root formation (Lelandais-Brière et al., 2007), so the interaction of *At*CNIH5 and *At*OCT1 likely takes place in the vascular tissues. Intriguingly, the *oct1* mutant exhibited enhanced root branching, phenocopying the higher lateral root density of *cnih5* (Lelandais-Brière et al., 2007). Although the heterologous expression of *At*OCT1 in yeast could transport carnitine, it remains to be determined which substrate *At*OCT1 transports that could negatively affect lateral root development. As *At*CNIH5 failed to interact with other manifest PSi transporters such as *At*HAK5, *At*SULTR1;3, and *At*VPE1 (**Fig. 6B**), the cargo recognition by *At*CNIH5 is specific through a yet-to-be-identified mechanism. *At*CNIH5 also interacted with the Golgi-localized *At*URGT6 and *At*GXM2. *AtGXM2* is a PSi gene and preferentially expressed in the root hair (Salazar-Henao and Schmidt, 2016), encoding a methyltransferase catalyzing 4-O-methylation of glucuronic acid (GlcA) side chains on the hemicellulose xylan (Lee et al., 2012; Urbanowicz et al., 2012; Yuan et al., 2014). On the other hand, *At*URGT6 contributes to the biosynthesis of rhamnogalacturonan-I (RG-I), which belongs to the pectin in mucilage and various plant cell wall types (Saez-Aguayo et al., 2020). Remarkably, various Golgi-localized proteins involved in plant cell wall modification such as *At*QUL2 (At2g03480) (Mouille et al., 2007), *At*GAE1 (At4g30440) (Mølhøj et al., 2004), *At*GAUT3 (At4g38270) (Sterling et al., 2006), and *At*TMN9 (At5g25100) (Hiroguchi et al., 2021), are downregulated in the Pi-limited *cnih5* roots (**Table 1**). A root-specific co-expression analysis revealed that early Pi-responsive genes participated in cell wall remodeling, thus addressing the significance of this process in response to Pi deficiency (Liao et al., 2011; Lin et al., 2011). Nevertheless, it awaits investigation whether *At*CNIH5 plays a critical role in Pi starvation-induced cell wall composition changes. We also identified the TP-localized *At*DTX21 and *At*DTX35 as the

potential cargoes of *At*CNIH5. Both proteins belong to the multidrug and toxic compound extrusion (MATE)-type transporter superfamily. *At*DTX21 is co-induced with the type III effectors secreted by *Pseudomonas syringae* and may mediate the detoxification of chlorinated herbicide atrazine (de Torres-Zabala et al., 2007; Ramel et al., 2007). *At*DTX35 is low Pi-responsive (Liu et al., 2016) and functions as a turgor-regulating chloride channel associated with root hair development (Zhang et al., 2017). More studies are required to unravel the physiological role of *At*DTX21 and *At*DTX35 in Pi starvation responses.

In summary, we employed a quantitative membrane proteomic approach to reveal the downregulation of *At*PHT1s and other membrane proteins associated with Pi starvation in *cnih5* root. Furthermore, we validated the interaction of *At*CNIH5 with their membrane cargoes at the post-ER compartments (**Fig. 9**) and showed that introducing the genomic GFP-*AtCNIH5* fragment boosted plant growth under Pi repletion and limitation. We propose that *At*CNIH5 acts as a Pi deficiency-inducible hub that controls the ER-to-Golgi trafficking of specific membrane cargoes, thereby improving plant fitness under suboptimal Pi availability.

Material and Method

Plant Material and Growth Conditions

Seeds of the *A. thaliana* wild-type (Columbia, Col-0) and *cnih5* (SAIL_256_B03) mutants used in this study were obtained from the Arabidopsis Biological Resource Center. Seeds were surface-sterilized and germinated on agar plates with one-half modified Hoagland's solution containing 1% sucrose and 0.7% Bacto agar and grown in the growth chamber at 22 °C with a 16-h light/8-h dark cycle. Pi-sufficient (+P; 250 μM Pi) or Pi-deficient (−P; 0 μM Pi) medium containing 1.2% agar was used for vertically grown plants.

Tissue Homogenization and Microsomal Protein Preparation

The roots of 11-day-old seedlings with five days of Pi starvation were harvested. Approximately 100 mg of root tissue was collected for each sample and stored at -80 °C for subsequent homogenization. The frozen samples were homogenized by TissueLyser II (QIAGEN). The method for microsomal protein extraction was modified from a

previous study (Abas and Luschnig, 2010), and all steps were performed on ice or 4 °C. Briefly, each sample was resuspended in 100 µl of extraction buffer (EB) containing 50 mM of hydroxyethyl piperazine ethane sulfonic acid (HEPES; Melford, pH 7.5), 25% (w/w 0.81 M) sucrose, 5% (v/v) glycerol, 10 mM of ethylenediaminetetraacetic acid (EDTA; Amresco, pH 8), 5 mM of KCl, 1 mM of dithiothreitol (DTT; Sigma), and 2× protease inhibitor cocktail (P9599, Sigma). An equivalent volume (100 µl) of 5% polyvinylpolypyrrolidone (PVPP; Sigma) suspension solution was used for each sample. The 5% PVPP was centrifuged at 2,000 g for 1 min at room temperature (RT). The precipitate was activated for 2 hours in an equivalent volume of activated solution containing 100 mM HEPES, 40% (w/w, 1.37 M) sucrose, 20 mM EDTA, and 10 mM KCl. The activated PVPP was centrifuged at 5,000 g for 1 min at RT, and the supernatant was removed. The activated PVPP pellet was mixed with the sample suspension and stood for 5 min, followed by centrifugation thrice. The first centrifugation was processed at 600 g for 3 min. The pellet was then re-extracted with 50 µl EB and centrifuged at 600 g for 3 min. The pellet was then re-extracted with 35 µl EB and centrifuged at 2,000 g for 30 s. After three times centrifugation, all the supernatants were combined and centrifuged again at 600 g for 3 min. The collected supernatant was diluted with an equivalent volume of ddH_2O to reach a final solution concentration containing 12–13% sucrose and centrifuged at 21,000 g for 90 min. The pellet was resuspended in washing buffer containing 10 mM HEPES, 5 mM EDTA, 1 mM phenylmethylsulfonyl fluoride (PMSF, Sigma), and 1× protease inhibitor cocktail and centrifuged at 21,000 g for 45 min. Finally, the pellet was stored at -80 °C for further analysis.

Protein Solubilization and In-Solution Digestion

Microsomal protein pellets were dissolved in 1% sodium 4-hexylphenylazosulfonate (Na-Azo, Excenen Pharmatech) in 100 mM triethylammonium bicarbonate (TEABC, Sigma) containing 2× protease inhibitor cocktail and 1 mM PMSF. The protein yield was determined by BCA assay (Pierce). For each sample, an equal amount of protein was reduced with 5 mM tris-(2-carboxyethyl)-phosphine (TCEP, Sigma) at 60 °C for 30 min, followed by cysteine-blocking with 10 mM methyl methanethiosulfonate (MMTS, Sigma) at 25 °C for 30 min. Samples were digested with sequencing-grade modified porcine trypsin (Promega) at 37 °C with shaking for 1 hour and then illuminated by 6W UV light

302 nm (UVP UVM-57, Analytik Jena) at 4 °C for 40 min. The digested proteins were then aliquot and stored at −20 °C until use.

Isobaric Tag for Relative and Absolute Quantitation (iTRAQ) Labeling and Peptide Separation

After trypsin digestion, 0.5 μg of peptides was subjected to 1D–LC–MS/MS without pre-fractionations to identify and quantify proteins as a quality control study. On the other hand, 10 μg of peptides was labeled using an iTRAQ Reagent-4 plex Multiplex Kit according to the manufacturer's instructions (Applied Biosystems) for 1 hour at RT. Two WT replicates were labeled with iTRAQ-114 and -115, and two *cnih5* replicates were labeled with iTRAQ-116 and -117, pooled and desalted by homemade C18-microcolumn (SOURCE 15RPC, GE Healthcare). The eluted peptides were dried by vacuum centrifugation. The desalted peptides were loaded onto a homemade strong cation exchange (SCX) column (Luna SCX 5μm, 0.5 × 120 mm) at a 2 μl/min flow rate for 60 min. The peptides were then fractionated to 24 fractions by eluting with 0 to 100% HPLC buffer B (1 M ammonium nitrate/25% acetonitrile/0.1% formic acid) using on-line two-dimensional high-performance liquid chromatography (2D-HPLC; Dionex Ultimate 3,000, Thermo Fisher). Each SCX fraction was diluted in-line before trapping onto a reverse-phase (RP) column (Zorbax 300SB-C18, 0.3 x 5 mm; Agilent Technologies). The peptides were then separated on a column (Waters BEH 1.7 μm, 100 μm I.D. × 10 cm with a 15 μm tip) using a multi-step gradient of HPLC buffer C (99.9% acetonitrile/0.1% formic acid) for 60 min with a flow rate of 0.3 μl/min.

Liquid Chromatography-Tandem Mass Spectrometry (LC-MS/MS) Analysis

The LC apparatus was coupled with a 2D linear ion trap mass spectrometer (LTQ-Orbitrap ELITE; Thermo Fisher) operated using Xcalibur 2.2 software (Thermo Fisher). The full-scan MS was performed in the Orbitrap over a range of 400 to 2,000 Da and a resolution of 120,000 at m/z 400. For proteome analysis, the 10 data-dependent MS/MS scan events (10 MS2 HCD) were followed by one MS scan for the 10 most abundant precursor ions in the preview MS scan. The m/z values selected for MS/MS were dynamically excluded for 80 sec with a relative mass window of 1 Da. The electrospray voltage was set to 1.8 kV, and the capillary temperature was set to 200 °C. MS and MS2

automatic gain control were set at 1,000 ms (full scan) and 300 ms (MS2 for HCD), or 3 × 10^6 ions (full scan) and 3 × 10^4 ions (MS2 for HCD) for maximum accumulated time or ions.

LC-MS Data Processing, Protein Identification and Quantification

Proteome Discoverer software (version 2.3, Thermo Fisher Scientific) was used for data analysis, incorporating the reporter ions quantifier node for iTRAQ quantification. The MS/MS spectra were searched against the SwissProt database using the Mascot search engine (Matrix Science, version 2.5). For peptide identification, a 10 ppm mass tolerance was allowed for intact peptide masses and 0.2 Da for HCD fragment ions, with allowance for two missed cleavages made from trypsin digestion. Variable modifications included oxidized methionine, acetylation (protein N-terminal), and iTRAQ-4plex (peptide N-terminal, K); methylthiolation (C) was considered a static modification. Peptide-spectrum matches (PSMs) were filtered based on high confidence and Mascot search engine rank 1 of peptide identification, ensuring an overall false discovery rate (FDR) below 0.01. Proteins with only a single peptide hit were removed. Quantitative protein data were exported from Proteome Discoverer using Integration Methods of the Most Confident Centroid with a 20 ppm tolerance. The data sets were analyzed by cross-comparison between four samples (ratio 1, 116:114; ratio 2, 117:114; ratio 3, 116:115, and ratio 4, 117:115). Protein ratios in each comparison group were normalized using the median ratio of each comparison group. A 1.25-fold cutoff was applied to identify differentially expressed proteins in each comparison group.

Protein Annotation and Interpretation

Transmembrane-related information was obtained through analysis using DeepTMHMM (https://dtu.biolib.com/DeepTMHMM) (Hallgren et al., 2022). Subcellular structure localization was analyzed by SUBA5 (https://suba.live/) (Hooper et al., 2016). For functional annotation of proteins, Gene Ontology (GO) and Kyoto Encyclopedia of Genes and Genomes (KEGG) enrichment analyses were determined by ShinyGO 0.80 (http://bioinformatics.sdstate.edu/go/) (Ge et al., 2019), in which *p*-values were computed using the hypergeometric test and multiple test correction was performed using the Benjamini–Hochberg method based on an FDR cut-off of 0.05. Only pathways with a

minimum of 10 genes were selected. Similar pathways that share 95% of their genes and 50% of the words in their names were eliminated according to the setting of ShinyGO 0.80. Dot plots of GO enrichment analysis were generated using the ggplot2 package (Wickham et al., 2016) in R version 4.3.1 (R Core Team, 2021), and the code was written using RStudio version 2023.06.2 (RStudio Team, 2020).

Microsomal protein extraction for immunoblot analysis

The MPs pellets were solubilized by 0.5% Azo in 25mM aqueous ammonium bicarbonate, pH 7.0 (919233; Sigma Aldrich). Alternatively, the low-speed pellet (LSP) was prepared as previously described (Yoshimoto et al., 2004), and microsomal protein was isolated using the Minute Plant Microsomal Membrane Extraction Kit (Invent, MM-018) according to the manual instructions. A 15–30 μg of MPs from each sample was loaded onto 4–12% Q-PAGE™ Bis-Tris Precast Gel (SMOBIO) or NuPAGE 4–12% Bis-Tris Gels (Thermo Fisher Scientific). Gel was transferred to polyvinylidene difluoride membranes (IPVH00010 Immobilon-P Membrane or ISEQ00010 Immobilon®-PSQ Membrane; Merck). Membrane was blocked with 1–2% BSA in 1× PBS solution with 0.2% Tween 20 (PBST, pH 7.2) at RT for 1 h, and rinsed two times with distilled water followed by hybridization with primary antibodies of *At*PHF1 (Huang et al., 2013), *At*PHO1 (Liu et al., 2012), *At*NRT2.1 (AS12 2612; Agrisera), and *At*CNIH5 at RT for 2 h or at 4 °C overnight in blocking solution. Polyclonal rabbit *At*CNIH5 antibody was raised against the region corresponding to the amino acid residues 96 to 114 (TELYNTNKWEQKKRVYKIG) by LTK BioLaboratories, Taiwan, and was affinity purified. The membrane was washed four times with 1× PBST for 5 min followed by hybridization with the horseradish peroxidase–conjugated secondary antibody (GTX213110-01 or GTX213111-01; GeneTex) in blocking solution at RT for 1 h. After four washes in 1× PBST for 5 min and a rinse with distilled water, chemiluminescent substrates (WesternBright ECL or Sirius; Advansta) were applied for signal detection.

Construct design and yeast split-ubiquitin assay

For constructing the yeast expression clones, the coding sequence (CDS) of the gene of interest (GOI), including the truncated *At*CNIH5 variants, was amplified by PCR, cloned into the pCR8/GW/TOPO vectors and sequenced. The pCR8/GW/TOPO construct

containing the CDS of *AtPHT1;1* was cloned as previously reported (Huang et al., 2013). The entry clones were recombined into NX32_GW (ABRC plasmid CD3-1737; Obrdlik et al., 2004) through LR reactions, resulting in Nub-fused or PLVCub-fused fragments. The PLVCub-*At*CNIH5 construct was generated as recently reported (Chiu et al., 2024). The Nub and PLVCub expression clones were sequentially transformed into the yeast THY.AP4 strain (ABRC CD3-808; Obrdlik et al., 2004). Fresh yeast colonies picked from yeast extract peptone dextrose adenine (YPDA) medium or synthetic complete (SC) medium without leucine (SC–L) were inoculated in the corresponding liquid medium and incubated overnight at 30 °C with shaking at 200 rpm. Overnight yeast culture was then diluted to OD_{600} = 0.2 and grew for another 4–6 h until OD_{600} reached 0.4–0.6. Yeast pellet was collected by centrifugation at 2,000×g at 4 °C for 10 min, washed with ddH_2O, and resuspended in Tris-EDTA/lithium acetate solution (TE/LiAc, 10 mM Tris-HCl [pH 8.0], 1 mM EDTA, and 0.1 M lithium acetate). Yeast transformants carrying the PLVCub-*At*CNIH*5/*truncated *At*CNIH5 variants or *At*PHT1;1-CubPLV construct were selected and maintained on SC–L for sequential transformation with NubWT (positive control), NubG (negative control), and GOI-NubG or NubG-GOI. Yeast transformants carrying the Nub and the PLVCub constructs were selected and maintained on SC medium without leucine and tryptophan (SC–LW). For the protein–protein interaction testing, yeast cells co-expressing PLVCub-*At*CNIH*5/*truncated *At*CNIH5 variants or *At*PHT1;1-CubPLV with GOI-NubG or NubG-GOI were grown on synthetic media lacking leucine, tryptophan, adenine, and histidine (SC–LWAH) with 500 μM methionine or on SC–LW containing 100 mg/L 5-bromo-4-chloro-3-indolyl-*β*-d-galactopyranoside (X-Gal) at 30 °C for 24–36 h. Primer sequences used are listed in **Supplementary Table S4**.

Construct design for split-GFP assays in *N. benthamiana* leaves and *Arabidopsis* transgenic plants

The *UBQ10:sXVE:* S10-*At*CNIH5 clone was obtained as recently reported (Chiu et al., 2024). For the transient expression of *At*PHT1;1-S11, *At*SOS-S11, *At*DTX21-S11, *At*DTX35-S11, *At*URGT6-S11, *At*OCT1-S11, *At*HAK5-S11, *At*VPE1-S11 and *At*SULTR1;3-S11, the CDS or the corresponding fragment was amplified by PCR and subcloned into *UBQ10:sXVE*: (MCS)-S11 (Addgene plasmid # 108179). For subcellular localization analysis of the protein of interest, either *UBQ10:sXVE:* S11-GFP1–9

(Addgene plasmid # 125665) or *UBQ10:sXVE:* GFP1–10 (Addgene plasmid # 125663) was co-expressed. For the tripartite split-GFP reconstitution, the constructs encoding S10-tagged and S11-tagged protein fusions were co-expressed in the presence of *UBQ10:sXVE*: GFP1–9 (Addgene plasmid # 108187). Co-expression with 3xHA-S11 (Addgene plasmid # 108238) was used as a negative control for protein–protein interaction. The brightness of the images for the protein–protein interaction was adjusted by a 20% increase and the contrast adjusted by a 20% decrease. Primer sequences used are listed in **Supplementary Table S4**. For the genomic GFP-*AtCNIH5* complemented plants (*AtCNIH5pro*: GFP-*AtCNIH5/cnih5*), the construct design was recently described (Chiu et al., 2024).

Agrobacterium tumefaciens-mediated infiltration of *N. benthamiana* leaves

Agrobacterium tumefaciens strain EHA105 harboring the expression constructs or p19 was cultured in Luria–Bertani (LB) medium with the appropriate antibiotics [gentamicin (50 μg ml^{-1}), rifampicin (5 μg ml^{-1}) or kanamycin (50 μg ml^{-1})]. Cells were resuspended in the infiltration medium containing 10 mM $MgCl_2$, 10 mM MES (pH 7.5), and 150 μM acetosyringone, and co-infiltrated to the true leaves of 3–5-week-old tobacco plants. For the β-estradiol-inducible split-GFP system, 36.7 μM *β*-estradiol was applied as previously described (Liu et al., 2018; Liu, 2021). Infiltrated leaves were collected 2 days post-infiltration (dpi) for confocal imaging.

Confocal microscopy

Confocal microscopy images were acquired using Zeiss LSM 800 (Zeiss) with objectives Plan-Apochromat 10×/0.45 M27, 20×/0.8 M27, and 40×/1.3 Oil DIC M27 in multi-track mode with line switching and averaging of two reading. Excitation/emission wavelengths were 488 nm/410–546 nm for GFP and 561 nm/656–700 nm for RFP and mCherry.

Chemical treatments

Acetosyringone (150 mM stock in DMSO; D134406; Sigma-Aldrich) was diluted to a final concentration of 150 μM in ddH_2O. *β*-estradiol (36.7 mM stock in ethanol; E2758; Sigma-Aldrich) was diluted to a final concentration of 36.7 μM in ddH_2O.

Accession Numbers

Sequence data from this article can be found in the Arabidopsis Genome Initiative under the following accession numbers: *At*CNIH5 (AT4G12090), *At*PHT1;1 (AT5G43350), *At*PHT1;2 (AT5G43370), *At*PHT1;5 (AT2G32830), *At*PHT1;7 (AT3G54700), *At*PHT1;9 (AT1G76430), *At*LRK10L-1.1 (AT1G18390), *At*GXM2 (AT4G09990), *At*SOS (AT1G26650), *At*DTX21 (AT1G33110), *At*DTX35 (AT4G25640), *At*URGT6 (AT1G34020), *At*OCT1 (AT1G73220), *At*HAK5 (AT4G13420), *At*VPE1 (AT3G47420), *At*SULTR1;3 (AT1G22150).

Supplementary Data

The following materials are available in the online version of this article.

Supplementary Fig. S1 Schematic workflow of Azo-solubilized microsomal protein extraction for iTRAQ-based quantitative proteomic analysis of *Arabidopsis* Pi-limited roots.

Supplementary Fig. S2 UV-Vis spectrum monitoring the degradation of 1% Azo as a function of UV irradiation time.

1% Azo in 100 mM TEABC buffer was 1: 200 diluted and subjected to measurement of the absorbance value at the wavelength of 305 nm following the UV irradiation with a 6W UV lamp.

Supplementary Fig. S3 Multiple marker abundance profiling (MMAP) of the identified proteins in Azo-solubilized microsomal protein extraction (MME) samples.

(A) Summary of label-free proteomic analysis of microsomal proteins in *Arabidopsis* WT and *cnih5* Pi-limited roots.

(B) Relative number of high confidence marker (hcm) proteins for each compartment. The relative number of distinct proteins for each compartment are displayed in the bar graph as a percentage of all unique proteins in Arabidopsis (Standard) or all proteins in the user sample (User).

(C) Relative protein abundance of high hcm proteins for each compartment. The Normalized Gator Abundance Factor (NGAF) scores for each protein is summed per

subcellular compartment according to the hcm assignments. The abundance-scaling factor for each compartment describes the skew between the standard observations in Arabidopsis (Standard) and the estimated abundance observation in the user sample. The NGAF scores for each protein in the user sample is multiplied by the compartmental scaling factor and summed per subcellular compartment according to the hcm list. The sums for each compartment are displayed in the bar graph as a percentage of the whole protein abundance (Standard) or all proteins in the total user sample (User).

Supplementary Fig. S4 GO enrichment analysis of the 372 upregulated proteins in Pi-limited *cnih5* roots.

Top 15 gene ontology (GO) terms for categories of molecular function (A), biological process (B), and cellular component (C).

(A) Dot plots of the top GO terms in enrichment analysis for categories of molecular function (MF), biological process (BP), and cellular component (CC) ranked by fold enrichment. Fold enrichment compares the sample frequency representing the number of genes inputted under each GO term to the background frequency of total genes annotated to the same term in *A. thaliana*. The size of the dot indicates the number of genes in each GO term. The more intense reddish color reflects a lower adjusted *p*-value shown by $-\log_{10}$(FDR).

(B) Hierarchical clustering tree of GO terms in (A). The relatedness of each GO term to each other was shown for the categories of molecular function (MF), biological process (BP), and cellular component (CC). Bigger blue dots indicate more significant adjusted *p*-value.

Supplementary Fig. S5 KEGG pathway enrichment analysis of the upregulated and downregulated proteins in Pi-limited *cnih5* roots.

Fold enrichment compares the sample frequency representing the number of genes inputted under KEGG term to the background frequency of total genes annotated to the same term in *A. thaliana*. The size of the dot indicates the number of genes in each KEGG term. The more intense reddish color reflects a lower adjusted *p*-value shown by $-\log_{10}$(FDR).

Supplementary Fig. S6 Analysis of the interaction of PLVCub-*At*CNIH5 with NubG-*At*SOS, NubG-*At*OCT1, NubG-*At*URGT6, NubG-*At*DTX21, and NubG-*At*DTX35 using the yeast split-ubiquitin system (SUS). The co-expression of PLVCub-*At*CNIH5 with NubWT and NubG are used as positive and negative controls, respectively. Yeast transformants were grown on synthetic medium without leucine and tryptophan (–LW; the left panel) or on synthetic medium lacking leucine, tryptophan, and adenine with 500 μM methionine (–LWAH; the middle panel) or on SC–LW containing 100 mg/L X-Gal (X-Gal; the right panel).

Supplementary Fig. S7 Amino acid sequence alignment of *Sc*Erv14 and *At*CNIHs.
The sequence alignment was performed using the Clustal Omega algorithm (Sievers et al., 2011) and visualized using Jalview version 2.11.4.0 (Waterhouse et al., 2009). The degree of amino acid conservation among the CNIHs is represented by a light-to-dark blue color gradient. The transmembrane domains (TMD) are boxed by solid lines. The putative cornichon, YLC, IFNLL, and acidic motifs are boxed by dotted lines. The protein sequences were retrieved from UniprotKB (Uniprot ID: *Sc*Erv14, P53173; *At*CNIH1, Q9C7D7; *At*CNIH2, Q3EDD7; *At*CNIH3, Q8GWT5; *At*CNIH4, Q84W04; *At*CNIH5, Q9SZ74).

Supplementary Fig. S8 Protein expression of the endogenous *At*CNIH5 in WT and GFP-*AtCNIH5* in the *AtCNIH5pro*: GFP-*AtCNIH5/cnih5* complementation (COM) plants under Pi deficiency.
Immunoblot analysis of *At*CNIH5 and GFP-*AtCNIH5* in the root of *Arabidopsis* 11-day-old WT and COM seedlings under Pi-deficient (–P, 0 μM KH_2PO_4, seven days of starvation) conditions. The bands of *At*CNIH5 and GFP-*AtCNIH5* are indicated by solid arrowhead and open arrowhead, respectively.

Supplementary Table S1. A list of the identified 4317 proteins in *Arabidopsis* Pi-limited WT and *cnih5* roots with GO enrichment analysis.
Detailed descriptions of our proteomic analysis, including the protein scores and mass, annotation, predicted transmembrane helices, quantification for the identified proteins, and a list of the 61 overlapped identified proteins between our datasets and the Pi

starvation root proteome by (Lan et al., 2012).

Supplementary Table S2. A list of the 372 upregulated and 106 downregulated proteins in Pi-limited *cnih5* roots with GO enrichment analysis.
Detailed descriptions, including annotation, predicted transmembrane helices, and quantification for the proteins identified in proteomic analysis.

Supplementary Table S3. A list of the 19 root Pi starvation-induced (PSi) genes encoding transporters.

Supplementary Table S4. Oligonucleotides used for plasmid constructs.

Acknowledgments

This work was supported by the Ministry of Science and Technology (MOST 108-2311-B-007-003-MY3) and the National Science and Technology Council (NSTC 112-2313-B-007-001-MY3). We acknowledge Ms. He-Ting Yang for cloning the CDS of *At*OCT1, *At*HAK5, *At*VPE1, and *At*SULTR1;3, and Mr. Po-Ruey Huang for cloning the constructs expressing the truncated *At*CNIH5 variants. We also thank Mr. Cheng-Da Tsai for testing the interaction of PLVCub-*At*CNIH5 with NubG-*At*PHT1;2, NubG-*At*PHT1;5, NubG-*At*PHT1;7 and NubG-*At*PHT1;9.

Author Contributions

T.-Y. L. conceived the project, designed the experiments, analyzed the experiments, and wrote the article. M.-H. T., J.-Y. W., H.-F. L., H.-X. C., C.-Y. C., and C.-A. L. performed and analyzed the experiments.

Figure Legends

Figure 1. Immunoblot analysis of root microsomal proteins extracted from WT, *cnih5*, and *pho2* mutants.
(A and B) Protein expression of *At*PHF1, *At*PHO1, and *At*NRT2.1 (A) and *At*CNIH5 (B) in the root of 11-day-old seedlings of *Arabidopsis* WT, *cnih5*, and *pho2* under Pi-

sufficient (+P) and Pi-deficient (–P, 0 μM KH_2PO_4, five days of starvation) conditions. The band of *At*CNIH5 is indicated by arrowhead. The relative protein expression level was normalized with the corresponding amido black staining and relative to the WT control. Error bars represent SE (n = 2–4). The applied extraction methods were shown as indicated.

Figure 2. Summary of proteomic analysis of microsomal proteins (MPs) in *Arabidopsis* WT and *cnih5* Pi-limited roots.

(A) Venn diagram for comparing MPs and transmembrane (TM) proteins of the 4317 identified proteins. Subcellular localization was analyzed by SUBA5. TM protein prediction or annotation was performed by deepTMHMM or UniprotKB.

(B) Distribution of subcellular localizations of the identified 4317 proteins analyzed by SUBA5. Note that not all proteins are restricted to a single subcellular location.

(C) Distribution of subcellular localizations of the 915 integral MPs among the identified 1231 TM proteins analyzed by SUBA5. Note that not all proteins are restricted to a single subcellular location.

Figure 3. Gene ontology (GO) analysis of the 4,317 identified proteins in iTRAQ-based proteomics of *Arabidopsis* WT and *cnih5* Pi-limited roots.

(A) Dot plots of the top GO terms in enrichment analysis for categories of molecular function (MF), biological process (BP), and cellular component (CC) ranked by fold enrichment. Fold enrichment compares the sample frequency representing the number of genes inputted under each GO term to the background frequency of total genes annotated to the same term in *A. thaliana*. The size of the dot indicates the number of genes in each GO term. The more intense reddish color reflects a lower adjusted *p*-value shown by $-\log_{10}$(FDR).

(B) Hierarchical clustering tree of GO terms in (A). The relatedness of each GO term to each other was shown for the categories of molecular function (MF), biological process (BP), and cellular component (CC). A bigger blue dot indicates a more significant adjusted *p*-value.

Figure 4. GO enrichment analysis of the 106 downregulated proteins in Pi-limited *cnih5*

roots.

(A) Dot plots of the top GO terms in enrichment analysis for categories of molecular function (MF), biological process (BP), and cellular component (CC) ranked by fold enrichment. Fold enrichment compares the sample frequency representing the number of genes inputted under each GO term to the background frequency of total genes annotated to the same term in *A. thaliana*. The size of the dot indicates the number of genes in each GO term. The more intense reddish color reflects a lower adjusted *p*-value shown by $-\log_{10}$(FDR).

(B) Hierarchical clustering tree of GO terms in (A). The relatedness of each GO term to each other was shown for the categories of molecular function (MF), biological process (BP), and cellular component (CC). Bigger blue dots indicate more significant adjusted *p*-value.

Figure 5. Analysis of the interaction of *At*CNIH5 with its potential ER cargoes by the yeast split-ubiquitin system.

(A) Co-expression of PLVCub-*At*CNIH5 with NubG-*At*PHT1;2, NubG-*At*PHT1;5, NubG-*At*PHT1;7, and NubG-*At*PHT1;9.

(B) Co-expression of PLVCub-*At*CNIH5 with *At*LRK10L-1.1-NubG, *At*SOS-NubG, *At*OCT1-NubG, *At*URGT6-NubG, NubG-*At*GXM2, *At*DTX21-NubG, and *At*DTX35-NubG. The co-expression of PLVCub-*At*CNIH5 with NubWT and NubG are used as positive and negative controls, respectively. Yeast transformants were grown on synthetic medium without leucine and tryptophan (–LW; the left panel) or on synthetic medium lacking leucine, tryptophan, adenine, and histidine with 500 μM methionine (–LWAH; middle panel) or on SC–LW containing 100 mg/L X-Gal (X-Gal; the right panel).

Figure 6. Analysis of the interaction of *At*CNIH5 with its potential ER cargoes by the tripartite split-GFP assay in *N. benthamiana* leaves.

(A and B) Subcellular localization (A) and protein–protein interaction analysis (B) of S10-*At*CNIH5, *At*PHT1;1-S11, 3xHA-S11, *At*SOS-S11, *At*OCT1-S11, *At*HAK5-S11, *At*SULTR1;3-S11, *At*URGT6-S11, *At*DTX21-S11, *At*DTX35-S11, and *At*VPE1-S11. The co-expression of S10-*At*CNIH5 with *At*PHT1;1-S11 and 3xHA-S11 are used as positive and negative controls, respectively. The percentage of laser power used for acquisition is

shown. Scale bars, 5 μm.

Figure 7. Analysis of the interaction of *At*PHT1;1 and the truncated *At*CNIH5 variants by the yeast split ubiquitin assay.

(A) Schematic diagram of full-length (FL) and truncated *At*CNIH5 variants. The length of the truncated variants are indicated by the number of residues. The transmembrane domains and the putative cornichon, YLC, IFNLL, and acidic motifs are shown. The black box, the transmembrane domain (TMD); the blue box, the cornichon motif; the green box, the YLC motif; the yellow box, the IFNLL motif. The red box, the acidic motif. The gray box shows the sequence alignment of the putative acidic motif of *Sc*Erv14 and *At*CNIHs. Noted that *At*CNIH5 has a shorter C-terminal tail carrying only one acidic residue D134.

(B) Co-expression of *At*PHT1;1-PLVCub with NubG-*At*CNIH5, NubG-*At*CNIH5 1–26, NubG-*At*CNIH5 1–49, NubG-*At*CNIH5 1–92, and NubG-*At*CNIH5 1–132. The co-expression of *At*PHT1;1-PLVCub with NubWT and NubG are used as positive and negative controls, respectively. Yeast transformants were grown on synthetic medium without leucine and tryptophan (–LW; the left panel) or on synthetic medium lacking leucine, tryptophan, adenine, and histidine with 500 μM methionine (–LWAH; middle panel) or on SC–LW containing 100 mg/L X-Gal (X-Gal; the right panel).

Figure 8. Increasing *in-situ At*CNIH5 expression/activity boosts plant growth.

The shoot and root fresh weight (FW) of *Arabidopsis* 11-day-old WT, *cnih5* and *AtCNIH5pro*: GFP-*AtCNIH5/cnih5* complementation (COM) lines under Pi-sufficient (+P, 250 μM KH_2PO_4), modest Pi-deficient (–P, 0 μM KH_2PO_4, three days of starvation or 50 μM KH_2PO_4, eleven days of starvation), and severe Pi-deficient (–P, 0 μM KH_2PO_4, eleven days of starvation) conditions. Data are visualized using BoxPlotR (Spitzer et al., 2014). Center lines show the medians; the central plus signs (+) show the means; box limits indicate the 25th and 75th percentiles; whiskers extend to the 5th and 95th percentiles, and data points are plotted as dots. Data significantly different from the other groups are indicated by different lowercase letters (n, pools of seedings from independent experiments; One-Way ANOVA, Duncan's test).

Figure 9. *At*CNIH5-mediated ER-to-Golgi transport of membrane proteins associated with Pi starvation responses in *Arabidopsis* root.

Under Pi starvation (−P), the transcripts of *CNIH5*, *PHT1* genes, *OCT1*, *GXM2*, and *DTX35* increase in *Arabidopsis* root cells (Liu et al., 2016). As an ER cargo receptor, CNIH5 assists the ER export of the newly synthesized PHT1s, LRK10L-1.1, SOS, OCT1, URGT6, GXM2, DTX21, and DTX35 and their loading into COPII vesicles, thus their corresponding subcellular destinations.

Table 1. List of the 31 downregulated microsomal transmembrane proteins in Pi-limited *cnih5* roots.

The normalized ratios compared the protein expression in Col-0_1, Col-0_2, *cnih5*_1, and *cnih5*_2 samples. The FDR adj. *p*-values were in the parentheses. The candidates highlighted in gray were selected for testing protein–protein interaction in this study. Subcellular localization is predicted or annotated by SUBA5, UniprotKB or experimental data.

Table 2. Summary of *At*PHT1s and *At*PHF1 expression in Pi-limited WT and *cnih5* roots.

The normalized ratios compared the protein expression in Col-0_1, Col-0_2, *cnih5*_1, and *cnih5*_2 samples. The FDR adj. *p*-values were in the parentheses.

References

Abas L, Luschnig C (2010) Maximum yields of microsomal-type membranes from small amounts of plant material without requiring ultracentrifugation. Anal. Biochem. **401:** 217-227

Arpat AB, Magliano P, Wege S, Rouached H, Stefanovic A, Poirier Y (2012) Functional expression of PHO1 to the Golgi and *trans*-Golgi network and its role in export of inorganic phosphate. Plant J. **71:** 479-491

Bayle V, Arrighi J-F, Creff A, Nespoulous C, Vialaret J, Rossignol M, Gonzalez E, Paz-Ares J, Nussaume L (2011) *Arabidopsis thaliana* High-Affinity Phosphate Transporters Exhibit Multiple Levels of Posttranslational Regulation. Plant Cell **23:** 1523-1535

Bökel C, Dass S, Wilsch-Bräuninger M, Roth S (2006) *Drosophila* Cornichon acts as cargo receptor for ER export of the TGFα-like growth factor Gurken. Development **133:** 459-470

Bowtell D, Fu P, Simon M, Senior P (1992) Identification of murine homologues of the Drosophila son of sevenless gene: potential activators of ras. Proc. Natl. Acad. Sci. **89:** 6511-6515

Brown KA, Chen B, Guardado-Alvarez TM, Lin Z, Hwang L, Ayaz-Guner S, Jin S, Ge Y (2019) A photocleavable surfactant for top-down proteomics. Nat. Methods **16:** 417-420

Brown KA, Tucholski T, Eken C, Knott S, Zhu Y, Jin S, Ge Y (2020) High-Throughput Proteomics Enabled by a Photocleavable Surfactant. Angew. Chem. Int. Ed. **59:** 8406-8410

Chen J, Wang Y, Wang F, Yang J, Gao M, Li C, Liu Y, Liu Y, Yamaji N, Ma JF, Paz-Ares J, Nussaume L, Zhang S, Yi K, Wu Z, Wu P (2015) The Rice CK2 Kinase Regulates Trafficking of Phosphate Transporters in Response to Phosphate Levels. Plant Cell **27:** 711-723

Chiu C-Y, Tsai C-D, Wang J-Y, Tsai M-H, Kanno S, Lung H-F, Liu T-Y (2024) Phosphate Starvation-Induced CORNICHON HOMOLOG 5 as Endoplasmic Reticulum Cargo Receptor for PHT1 Transporters in *Arabidopsis*. bioRxiv**:** 2024.2006.2020.599911

Chopin F, Wirth J, Dorbe M-F, Lejay L, Krapp A, Gojon A, Daniel-Vedele F (2007) The Arabidopsis nitrate transporter AtNRT2.1 is targeted to the root plasma membrane. Plant Physiol. Biochem. **45:** 630-635

de Torres-Zabala M, Truman W, Bennett MH, Lafforgue G, Mansfield JW, Rodriguez Egea P, Bögre L, Grant M (2007) *Pseudomonas syringae* pv. *tomato* hijacks the *Arabidopsis* abscisic acid signalling pathway to cause disease. EMBO J. **26:** 1434-1443

Evenson KJ, Post-Beittenmiller D (1995) Fatty Acid-Elongating Activity in Rapidly Expanding Leek Epidermis. Plant Physiol. **109:** 707-716

Ge SX, Jung D, Yao R (2019) ShinyGO: a graphical gene-set enrichment tool for animals and plants. Bioinformatics **36:** 2628-2629

González E, Solano R, Rubio V, Leyva A, Paz-Ares J (2005) PHOSPHATE TRANSPORTER TRAFFIC FACILITATOR1 Is a Plant-Specific SEC12-Related Protein That Enables the Endoplasmic Reticulum Exit of a High-Affinity Phosphate Transporter in *Arabidopsis*. Plant Cell **17:** 3500-3512

Hallgren J, Tsirigos KD, Pedersen MD, Almagro Armenteros JJ, Marcatili P,

Nielsen H, Krogh A, Winther O (2022) DeepTMHMM predicts alpha and beta transmembrane proteins using deep neural networks. bioRxiv**:** 2022.2004.2008.487609

Harmel N, Cokic B, Zolles G, Berkefeld H, Mauric V, Fakler B, Stein V, Klöcker N (2012) AMPA Receptors Commandeer an Ancient Cargo Exporter for Use as an Auxiliary Subunit for Signaling. PLoS One **7:** e30681

Hiroguchi A, Sakamoto S, Mitsuda N, Miwa K (2021) Golgi-localized membrane protein AtTMN1/EMP12 functions in the deposition of rhamnogalacturonan II and I for cell growth in Arabidopsis. J. Exp. Bot. **72:** 3611-3629

Hooper CM, Castleden IR, Tanz SK, Aryamanesh N, Millar AH (2016) SUBA4: the interactive data analysis centre for Arabidopsis subcellular protein locations. Nucleic Acids Res. **45:** D1064-D1074

Huang T-K, Han C-L, Lin S-I, Chen Y-J, Tsai Y-C, Chen Y-R, Chen J-W, Lin W-Y, Chen P-M, Liu T-Y, Chen Y-S, Sun C-M, Chiou T-J (2013) Identification of Downstream Components of Ubiquitin-Conjugating Enzyme PHOSPHATE2 by Quantitative Membrane Proteomics in Arabidopsis Roots. The Plant Cell **25:** 4044-4060

Krogh A, Larsson B, von Heijne G, Sonnhammer ELL (2001) Predicting transmembrane protein topology with a hidden markov model: application to complete genomes. J. Mol. Biol. **305:** 567-580

Lan P, Li W, Schmidt W (2012) Complementary Proteome and Transcriptome Profiling in Phosphate-deficient Arabidopsis Roots Reveals Multiple Levels of Gene Regulation. Mol. Cell. Proteomics **11:** 1156-1166

Lee C, Teng Q, Zhong R, Yuan Y, Haghighat M, Ye Z-H (2012) Three Arabidopsis DUF579 Domain-Containing GXM Proteins are Methyltransferases Catalyzing 4-*O*-Methylation of Glucuronic Acid on Xylan. Plant Cell Physiol. **53:** 1934-1949

Lee S-B, Jung S-J, Go Y-S, Kim H-U, Kim J-K, Cho H-J, Park OK, Suh M-C (2009) Two Arabidopsis 3-ketoacyl CoA synthase genes, *KCS20* and *KCS2/DAISY*, are functionally redundant in cuticular wax and root suberin biosynthesis, but differentially controlled by osmotic stress. Plant J. **60:** 462-475

Lelandais-Brière C, Jovanovic M, Torres GAM, Perrin Y, Lemoine R, Corre-Menguy F, Hartmann C (2007) Disruption of *AtOCT1*, an organic cation transporter gene, affects root development and carnitine-related responses in Arabidopsis. Plant J. **51:** 154-164

Liao Y-Y, Buckhout TJ, Schmidt W (2011) Phosphate deficiency-induced cell wall remodeling. Plant Signal. Behav. **6:** 700-702

Lim CW, Yang SH, Shin KH, Lee SC, Kim SH (2015) The AtLRK10L1.2, *Arabidopsis* ortholog of wheat LRK10, is involved in ABA-mediated signaling and drought resistance. Plant Cell Rep. **34:** 447-455

Lin W-D, Liao Y-Y, Yang TJW, Pan C-Y, Buckhout TJ, Schmidt W (2011) Coexpression-Based Clustering of Arabidopsis Root Genes Predicts Functional Modules in Early Phosphate Deficiency Signaling. Plant Physiol. **155:** 1383-1402

Lin W-Y, Huang T-K, Chiou T-J (2013) NITROGEN LIMITATION ADAPTATION, a Target of MicroRNA827, Mediates Degradation of Plasma Membrane–Localized Phosphate Transporters to Maintain Phosphate Homeostasis in *Arabidopsis*. Plant Cell **25:** 4061-4074

Liu T-Y (2021) Using Tripartite Split-sfGFP for the Study of Membrane Protein–Protein Interactions. *In* JJ Sanchez-Serrano, J Salinas, eds, Arabidopsis Protocols.

Springer US, New York, NY, pp 323-336
Liu T-Y, Chou W-C, Chen W-Y, Chu C-Y, Dai C-Y, Wu P-Y (2018) Detection of membrane protein–protein interaction *in planta* based on dual-intein-coupled tripartite split-GFP association. Plant J. **94:** 426-438
Liu T-Y, Huang T-K, Tseng C-Y, Lai Y-S, Lin S-I, Lin W-Y, Chen J-W, Chiou T-J (2012) PHO2-Dependent Degradation of PHO1 Modulates Phosphate Homeostasis in *Arabidopsis*. Plant Cell **24:** 2168-2183
Liu T-Y, Huang T-K, Yang S-Y, Hong Y-T, Huang S-M, Wang F-N, Chiang S-F, Tsai S-Y, Lu W-C, Chiou T-J (2016) Identification of plant vacuolar transporters mediating phosphate storage. Nat. Commun. **7:** 11095
Mølhøj M, Verma R, Reiter W-D (2004) The Biosynthesis of d-Galacturonate in Plants. Functional Cloning and Characterization of a Membrane-Anchored UDP-d-Glucuronate 4-Epimerase from Arabidopsis. Plant Physiol. **135:** 1221-1230
Mouille G, Ralet M-C, Cavelier C, Eland C, Effroy D, Hématy K, McCartney L, Truong HN, Gaudon V, Thibault J-F, Marchant A, Höfte H (2007) Homogalacturonan synthesis in *Arabidopsis thaliana* requires a Golgi-localized protein with a putative methyltransferase domain. Plant J. **50:** 605-614
Nakanishi H, Suda Y, Neiman AM (2007) Erv14 family cargo receptors are necessary for ER exit during sporulation in *Saccharomyces cerevisiae*. J. Cell Sci. **120:** 908-916
Nguyen TV, Gupta R, Annas D, Yoon J, Kim Y-J, Lee GH, Jang JW, Park KH, Rakwal R, Jung K-H, Min CW, Kim ST (2021) An Integrated Approach for the Efficient Extraction and Solubilization of Rice Microsomal Membrane Proteins for High-Throughput Proteomics. Front. Plant Sci. **12**
Nussaume L, Kanno S, Javot H, Marin E, Nakanishi TM, Thibaud M-C (2011) Phosphate Import in Plants: Focus on the PHT1 Transporters. Front. Plant Sci. **2**
Obrdlik P, El-Bakkoury M, Hamacher T, Cappellaro C, Vilarino C, Fleischer C, Ellerbrok H, Kamuzinzi R, Ledent V, Blaudez D, Sanders D, Revuelta JL, Boles E, André B, Frommer WB (2004) K^+ channel interactions detected by a genetic system optimized for systematic studies of membrane protein interactions. Proc. Natl. Acad. Sci. **101:** 12242-12247
Pagant S, Wu A, Edwards S, Diehl F, Miller Elizabeth A (2015) Sec24 Is a Coincidence Detector that Simultaneously Binds Two Signals to Drive ER Export. Curr. Biol. **25:** 403-412
Park BS, Seo JS, Chua N-H (2014) NITROGEN LIMITATION ADAPTATION Recruits PHOSPHATE2 to Target the Phosphate Transporter PT2 for Degradation during the Regulation of *Arabidopsis* Phosphate Homeostasis. Plant Cell **26:** 454-464
Poirier Y, Bucher M (2002) Phosphate Transport and Homeostasis in Arabidopsis. The Arabidopsis Book **2002**
Poirier Y, Jaskolowski A, Clúa J (2022) Phosphate acquisition and metabolism in plants. Curr. Biol. **32:** R623-R629
Powers J, Barlowe C (1998) Transport of Axl2p Depends on Erv14p, an ER–Vesicle Protein Related to the *Drosophila cornichon* Gene Product. J. Cell Biol. **142:** 1209-1222
Powers J, Barlowe C (2002) Erv14p Directs a Transmembrane Secretory Protein into COPII-coated Transport Vesicles. Mol. Biol. Cell **13:** 880-891
R Core Team (2021) R: A Language and Environment for Statistical Computing. R

Foundation for Statistical Computing

Ramel F, Sulmon C, Cabello-Hurtado F, Taconnat L, Martin-Magniette M-L, Renou J-P, El Amrani A, Couée I, Gouesbet G (2007) Genome-wide interacting effects of sucrose and herbicide-mediated stress in *Arabidopsis thaliana*: novel insights into atrazine toxicity and sucrose-induced tolerance. BMC Genom. **8:** 450

Rosas-Santiago P, Lagunas-Gómez D, Barkla BJ, Vera-Estrella R, Lalonde S, Jones A, Frommer WB, Zimmermannova O, Sychrová H, Pantoja O (2015) Identification of rice cornichon as a possible cargo receptor for the Golgi-localized sodium transporter OsHKT1;3. J. Exp. Bot. **66:** 2733-2748

Rosas-Santiago P, Lagunas-Gomez D, Yáñez-Domínguez C, Vera-Estrella R, Zimmermannová O, Sychrová H, Pantoja O (2017) Plant and yeast cornichon possess a conserved acidic motif required for correct targeting of plasma membrane cargos. Biochim. Biophys. Acta **1864:** 1809-1818

RStudio Team (2020) RStudio: Integrated Development Environment for R. RStudio, PBC

Saez-Aguayo S, Parra-Rojas JP, Sepúlveda-Orellana P, Celiz-Balboa J, Arenas-Morales V, Sallé C, Salinas-Grenet H, Largo-Gosens A, North HM, Ralet M-C, Orellana A (2020) Transport of UDP-rhamnose by URGT2, URGT4, and URGT6 modulates rhamnogalacturonan-I length. Plant Physiol. **185:** 914-933

Salazar-Henao JE, Schmidt W (2016) An Inventory of Nutrient-Responsive Genes in *Arabidopsis* Root Hairs. Front. Plant Sci. **7**

Sievers F, Wilm A, Dineen D, Gibson TJ, Karplus K, Li W, Lopez R, McWilliam H, Remmert M, Söding J, Thompson JD, Higgins DG (2011) Fast, scalable generation of high-quality protein multiple sequence alignments using Clustal Omega. Mol. Syst. Biol. **7:** 539

Spitzer M, Wildenhain J, Rappsilber J, Tyers M (2014) BoxPlotR: a web tool for generation of box plots. Nat. Methods **11:** 121-122

Sterling JD, Atmodjo MA, Inwood SE, Kumar Kolli VS, Quigley HF, Hahn MG, Mohnen D (2006) Functional identification of an *Arabidopsis* pectin biosynthetic homogalacturonan galacturonosyltransferase. Proc. Natl. Acad. Sci. **103:** 5236-5241

The UniProt Consortium (2023) UniProt: the Universal Protein Knowledgebase in 2023. Nucleic Acids Res. **51:** D523-D531

Tian T, Liu Y, Yan H, You Q, Yi X, Du Z, Xu W, Su Z (2017) agriGO v2.0: a GO analysis toolkit for the agricultural community, 2017 update. Nucleic Acids Res. **45:** W122-W129

Urbanowicz BR, Peña MJ, Ratnaparkhe S, Avci U, Backe J, Steet HF, Foston M, Li H, O'Neill MA, Ragauskas AJ, Darvill AG, Wyman C, Gilbert HJ, York WS (2012) 4-*O*-methylation of glucuronic acid in *Arabidopsis* glucuronoxylan is catalyzed by a domain of unknown function family 579 protein. Proc. Natl. Acad. Sci. **109:** 14253-14258

Wang X, Liang S (2012) Sample preparation for the analysis of membrane proteomes by mass spectrometry. Protein Cell **3:** 661-668

Waterhouse AM, Procter JB, Martin DMA, Clamp M, Barton GJ (2009) Jalview Version 2—a multiple sequence alignment editor and analysis workbench. Bioinformatics **25:** 1189-1191

Wei L, Liu L, Chen Z, Huang Y, Yang L, Wang P, Xue S, Bie Z (2023) CmCNIH1

improves salt tolerance by influencing the trafficking of CmHKT1;1 in pumpkin. Plant J. **114:** 1353-1368

Wickham H, Chang W, Henry L, Lin Pedersen T, Takahashi K, Wilke C, Woo K, Yutani H, Dunnington D, van den Brand T (2016) ggplot2: Elegant Graphics for Data Analysis. Springer-Verlag New York

Wu X, Lai Y, Rao S, Lv L, Ji M, Han K, Weng J, Lu Y, Peng J, Lin L, Wu G, Chen J, Yan F, Zheng H (2021) Genome-Wide Identification Reveals That *Nicotiana benthamiana* Hypersensitive Response (HR)-Like Lesion Inducing Protein 4 (NbHRLI4) Mediates Cell Death and Salicylic Acid-Dependent Defense Responses to Turnip Mosaic Virus. Front. Plant Sci. **12**

Wudick MM, Portes MT, Michard E, Rosas-Santiago P, Lizzio MA, Nunes CO, Campos C, Santa Cruz Damineli D, Carvalho JC, Lima PT, Pantoja O, Feijó JA (2018) CORNICHON sorting and regulation of GLR channels underlie pollen tube Ca^{2+} homeostasis. Science **360:** 533-536

Yáñez-Domínguez C, Lagunas-Gómez D, Torres-Cifuentes DM, Bezanilla M, Pantoja O (2023) A cornichon protein controls polar localization of the PINA auxin transporter in *Physcomitrium patens*. Development **150**

Yang Z, Yang J, Wang Y, Wang F, Mao W, He Q, Xu J, Wu Z, Mao C (2020) PROTEIN PHOSPHATASE95 Regulates Phosphate Homeostasis by Affecting Phosphate Transporter Trafficking in Rice. Plant Cell **32:** 740-757

Yoshimoto K, Hanaoka H, Sato S, Kato T, Tabata S, Noda T, Ohsumi Y (2004) Processing of ATG8s, Ubiquitin-Like Proteins, and Their Deconjugation by ATG4s Are Essential for Plant Autophagy. Plant Cell **16:** 2967-2983

Yuan Y, Teng Q, Lee C, Zhong R, Ye Z-H (2014) Modification of the degree of 4-*O*-methylation of secondary wall glucuronoxylan. Plant Sci. **219-220:** 42-50

Zhang H, Zhao F-G, Tang R-J, Yu Y, Song J, Wang Y, Li L, Luan S (2017) Two tonoplast MATE proteins function as turgor-regulating chloride channels in *Arabidopsis*. Proc. Natl. Acad. Sci. **114:** E2036-E2045

Zheng J, Yao L, Zeng X, Wang B, Pan L (2023) *ERV14* receptor impacts mycelial growth via its interactions with cell wall synthase and transporters in *Aspergillus niger*. Front. Microbiol. **14**

Zhou M, Zhu S, Mo X, Guo Q, Li Y, Tian J, Liang C (2022) Proteomic Analysis Dissects Molecular Mechanisms Underlying Plant Responses to Phosphorus Deficiency. Cells **11:** 651

Zimmermannová O, Felcmanová K, Rosas-Santiago P, Papoušková K, Pantoja O, Sychrová H (2019) Erv14 cargo receptor participates in regulation of plasma-membrane potential, intracellular pH and potassium homeostasis via its interaction with K^+-specific transporters Trk1 and Tok1. Biochim. Biophys. Acta **1866:** 1376-1388

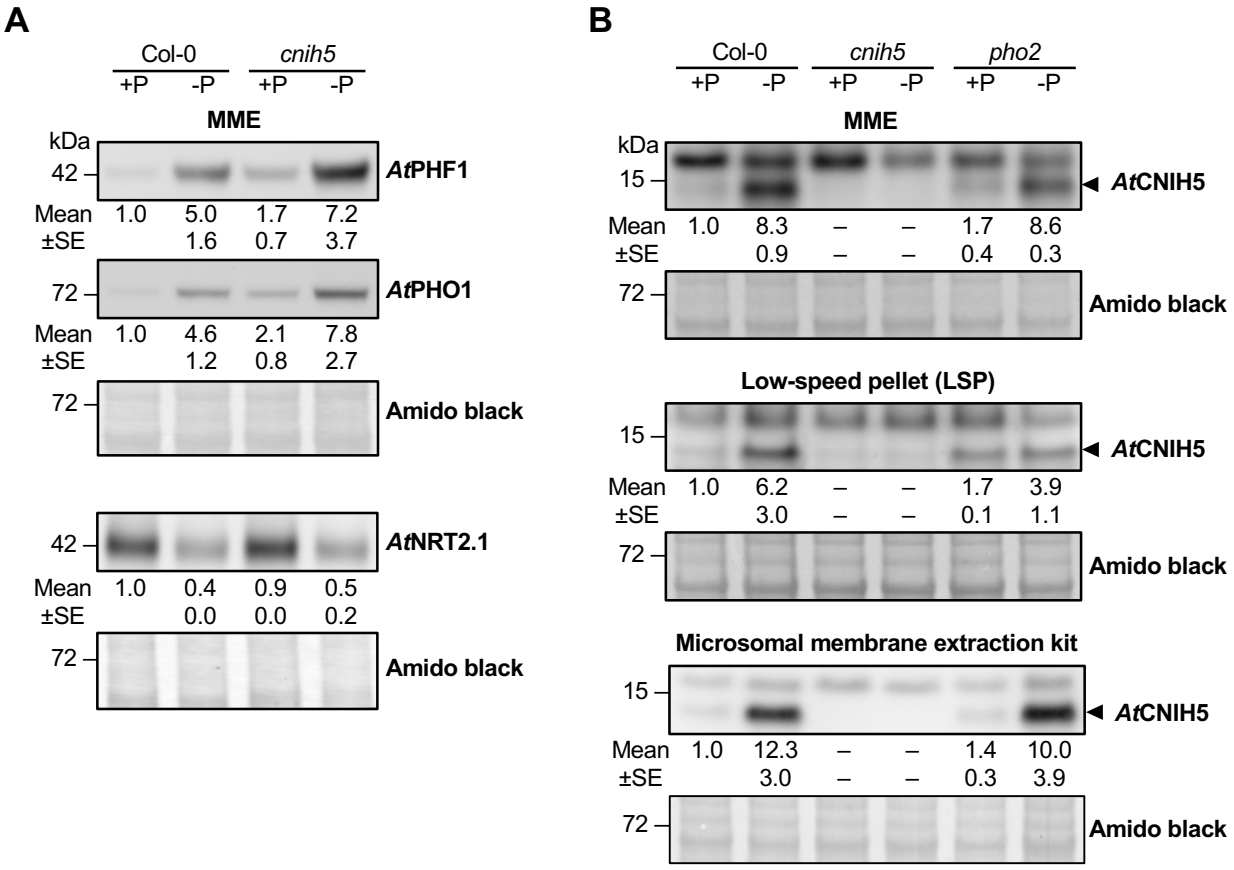

Figure 1. Immunoblot analysis of root microsomal proteins extracted from WT, *cnih5*, and *pho2* mutants.
(A and B) Protein expression of *At*PHF1, *At*PHO1, and *At*NRT2.1 (A) and *At*CNIH5 (B) in the root of 11-day-old seedlings of *Arabidopsis* WT, *cnih5*, and *pho2* under Pi-sufficient (+P) and Pi-deficient (–P, 0 μM KH_2PO_4, five days of starvation) conditions. The band of *At*CNIH5 is indicated by arrowhead. The relative protein expression level was normalized with the corresponding amido black staining and relative to the WT control. Error bars represent SE (n = 2–4). The applied extraction methods were shown as indicated.

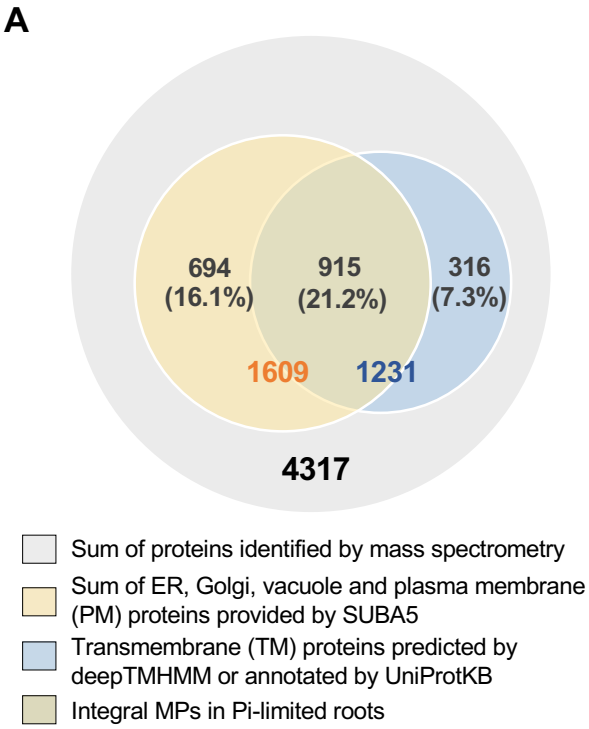

B

Distribution of subcellular localizations of the 4317 identified proteins

ER	Golgi	vacuole	PM
338 (7.8%)	435 (10.1%)	190 (4.4%)	698 (16.2%)

C

Distribution of subcellular localizations of the 915 integral MPs

ER	Golgi	vacuole	PM
237 (19.3%)	193 (15.7%)	119 (9.7%)	390 (31.7%)

Figure 2. Summary of proteomic analysis of microsomal proteins (MPs) in *Arabidopsis* WT and *cnih5* Pi-limited roots.
(A) Venn diagram for comparing MPs and transmembrane (TM) proteins of the 4317 identified proteins. Subcellular localization was analyzed by SUBA5. TM protein prediction or annotation was performed by deepTMHMM or UniprotKB.
(B) Distribution of subcellular localizations of the identified 4317 proteins analyzed by SUBA5. Note that not all proteins are restricted to a single subcellular location.
(C) Distribution of subcellular localizations of the 915 integral MPs among the identified 1231 TM proteins analyzed by SUBA5. Note that not all proteins are restricted to a single subcellular location.

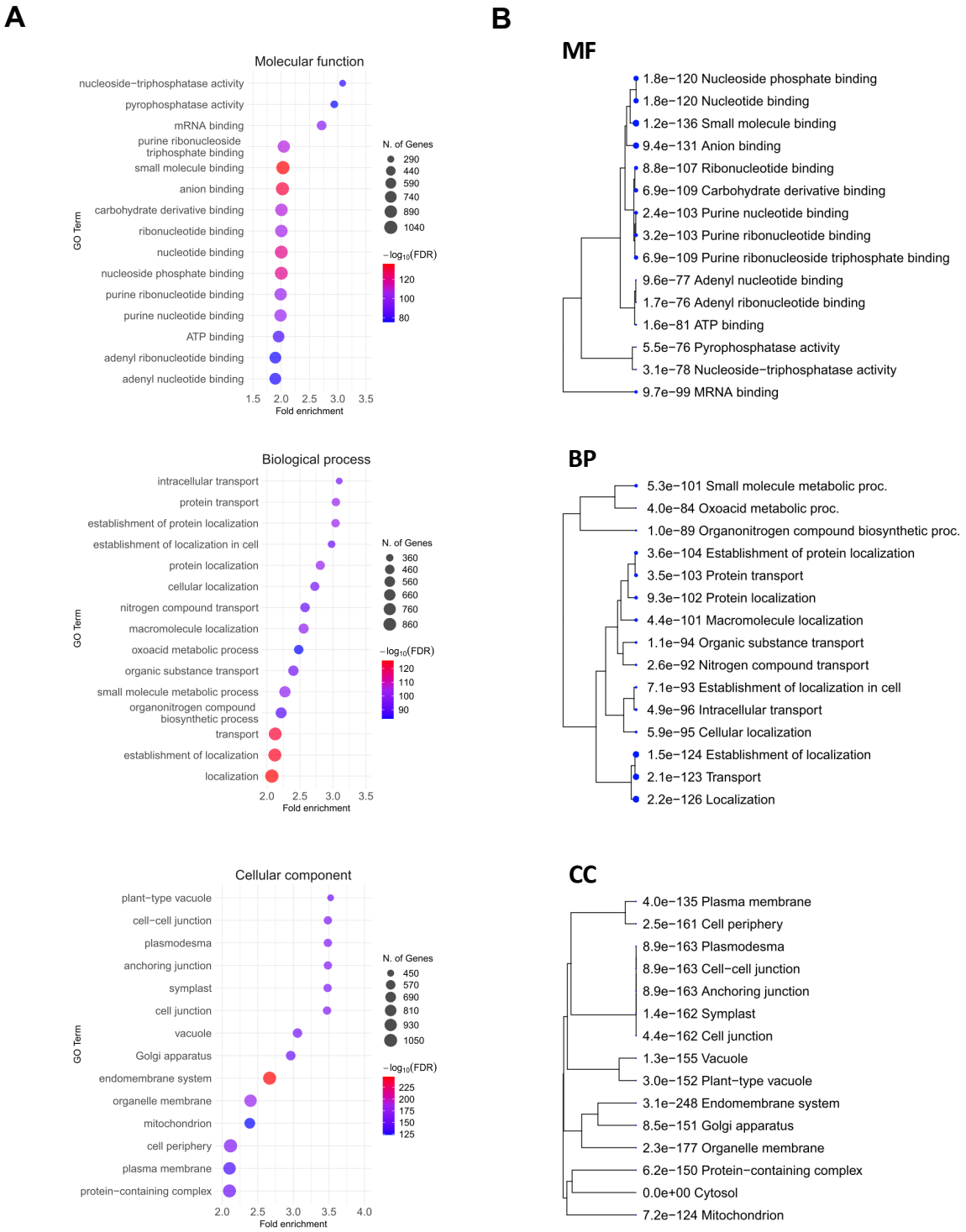

Figure 3. Gene ontology (GO) analysis of the 4,317 identified proteins in iTRAQ-based proteomics of *Arabidopsis* WT and *cnih5* Pi-limited roots.

(A) Dot plots of the top GO terms in enrichment analysis for categories of molecular function (MF), biological process (BP), and cellular component (CC) ranked by fold enrichment. Fold enrichment compares the sample frequency representing the number of genes inputted under each GO term to the background frequency of total genes annotated to the same term in *A. thaliana*. The size of the dot indicates the number of genes in each GO term. The more intense reddish color reflects a lower adjusted *p*-value shown by $-\log_{10}$(FDR).

(B) Hierarchical clustering tree of GO terms in (A). The relatedness of each GO term to each other was shown for the categories of molecular function (MF), biological process (BP), and cellular component (CC). A bigger blue dot indicates a more significant adjusted *p*-value.

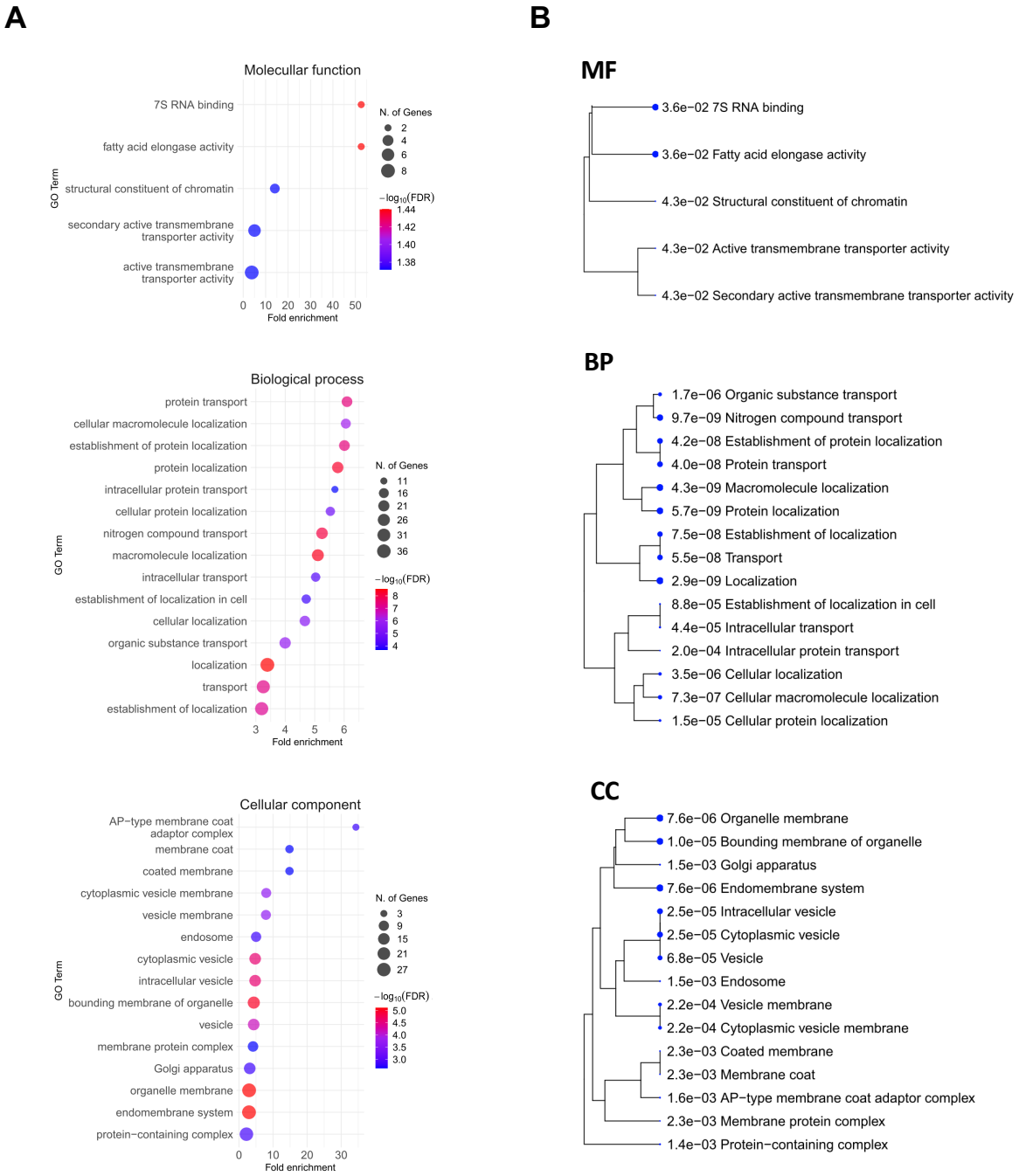

Figure 4. GO analysis of the 106 downregulated proteins in Pi-limited *cnih5* roots.
(A) Dot plots of the top GO terms in enrichment analysis for categories of molecular function (MF), biological process (BP), and cellular component (CC) ranked by fold enrichment. Fold enrichment compares the sample frequency representing the number of genes inputted under each GO term to the background frequency of total genes annotated to the same term in *A. thaliana*. The size of the dot indicates the number of genes in each GO term. The more intense reddish color reflects a lower adjusted *p*-value shown by $-\log_{10}$(FDR).
(B) Hierarchical clustering tree of GO terms in (A). The relatedness of each GO term to each other was shown for the categories of molecular function (MF), biological process (BP), and cellular component (CC). Bigger blue dots indicate more significant adjusted *p*-value.

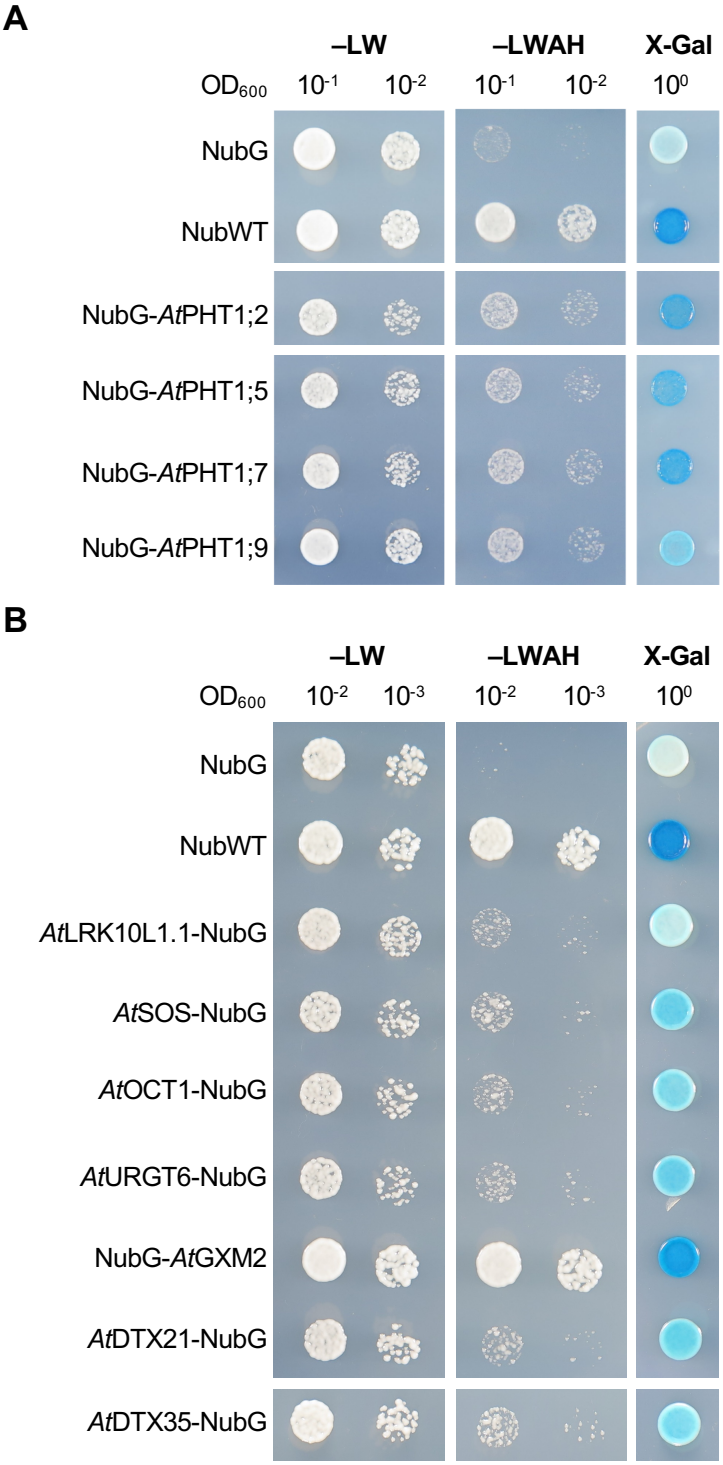

Figure 5. Analysis of the interaction of *At*CNIH5 with its potential ER cargoes by the yeast split-ubiquitin system.
(A) Co-expression of PLVCub-*At*CNIH5 with NubG-*At*PHT1;2, NubG-*At*PHT1;5, NubG-*At*PHT1;7, and NubG-*At*PHT1;9.
(B) Co-expression of PLVCub-*At*CNIH5 with *At*LRK10L-1.1-NubG, *At*SOS-NubG, *At*OCT1-NubG, *At*URGT6-NubG, NubG-*At*GXM2, *At*DTX21-NubG, and *At*DTX35-NubG. The co-expression of PLVCub-*At*CNIH5 with NubWT and NubG are used as positive and negative controls, respectively. Yeast transformants were grown on synthetic medium without leucine and tryptophan (–LW; the left panel) or on synthetic medium lacking leucine, tryptophan, adenine, and histidine with 500 μM methionine (–LWAH; middle panel) or on SC–LW containing 100 mg/L X-Gal (X-Gal; the right panel).

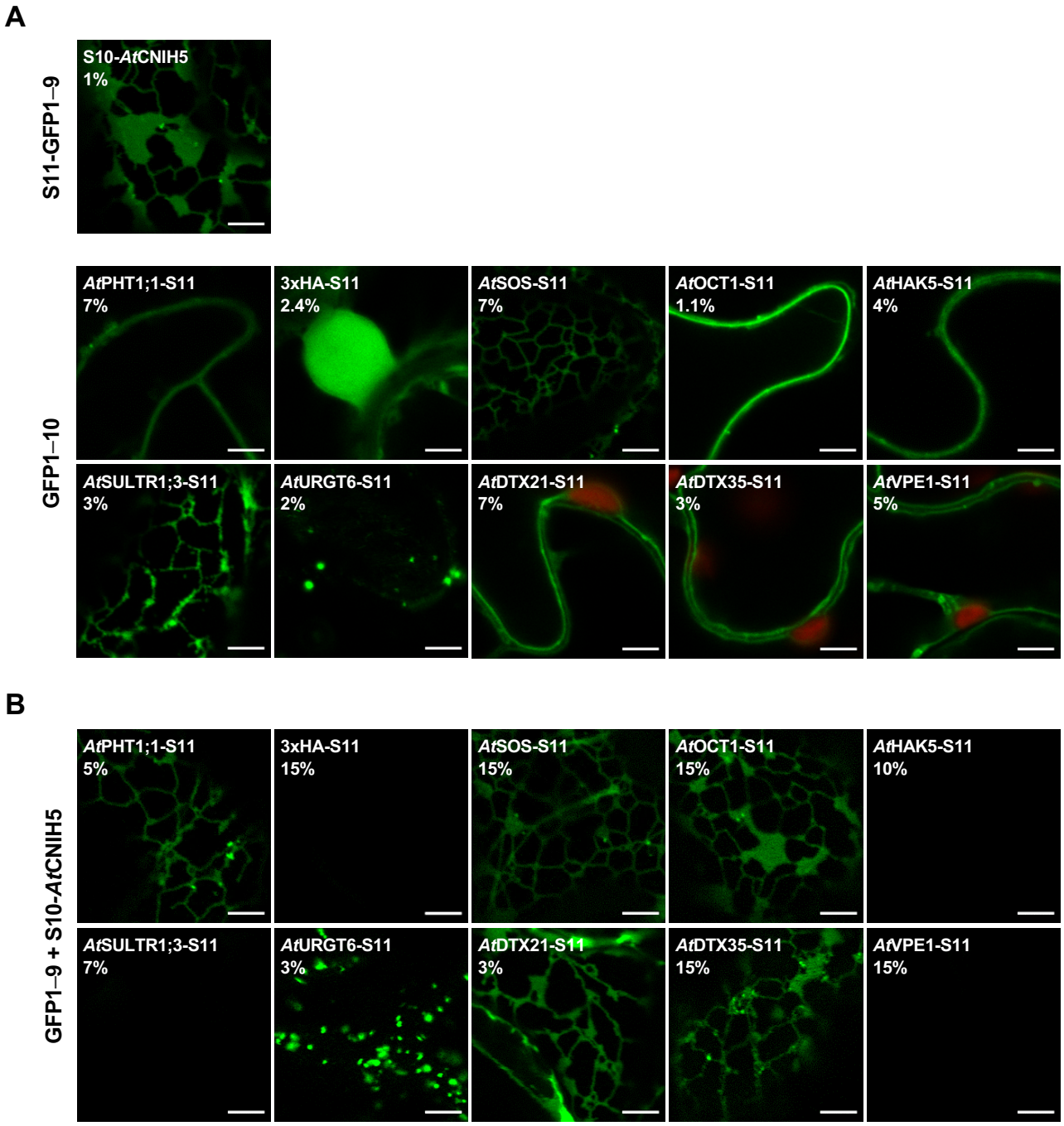

Figure 6. Analysis of the interaction of *At*CNIH5 with its potential ER cargoes by the tripartite split-GFP assay in *N. benthamiana* leaves.
(A and B) Subcellular localization (A) and protein–protein interaction analysis (B) of S10-*At*CNIH5, *At*PHT1;1-S11, 3xHA-S11, *At*SOS-S11, *At*OCT1-S11, *At*HAK5-S11, *At*SULTR1;3-S11, *At*URGT6-S11, *At*DTX21-S11, *At*DTX35-S11, and *At*VPE1-S11. The co-expression of S10-*At*CNIH5 with *At*PHT1;1-S11 and 3xHA-S11 are used as positive and negative controls, respectively. The percentage of laser power used for acquisition is shown. Scale bars, 5 μm.

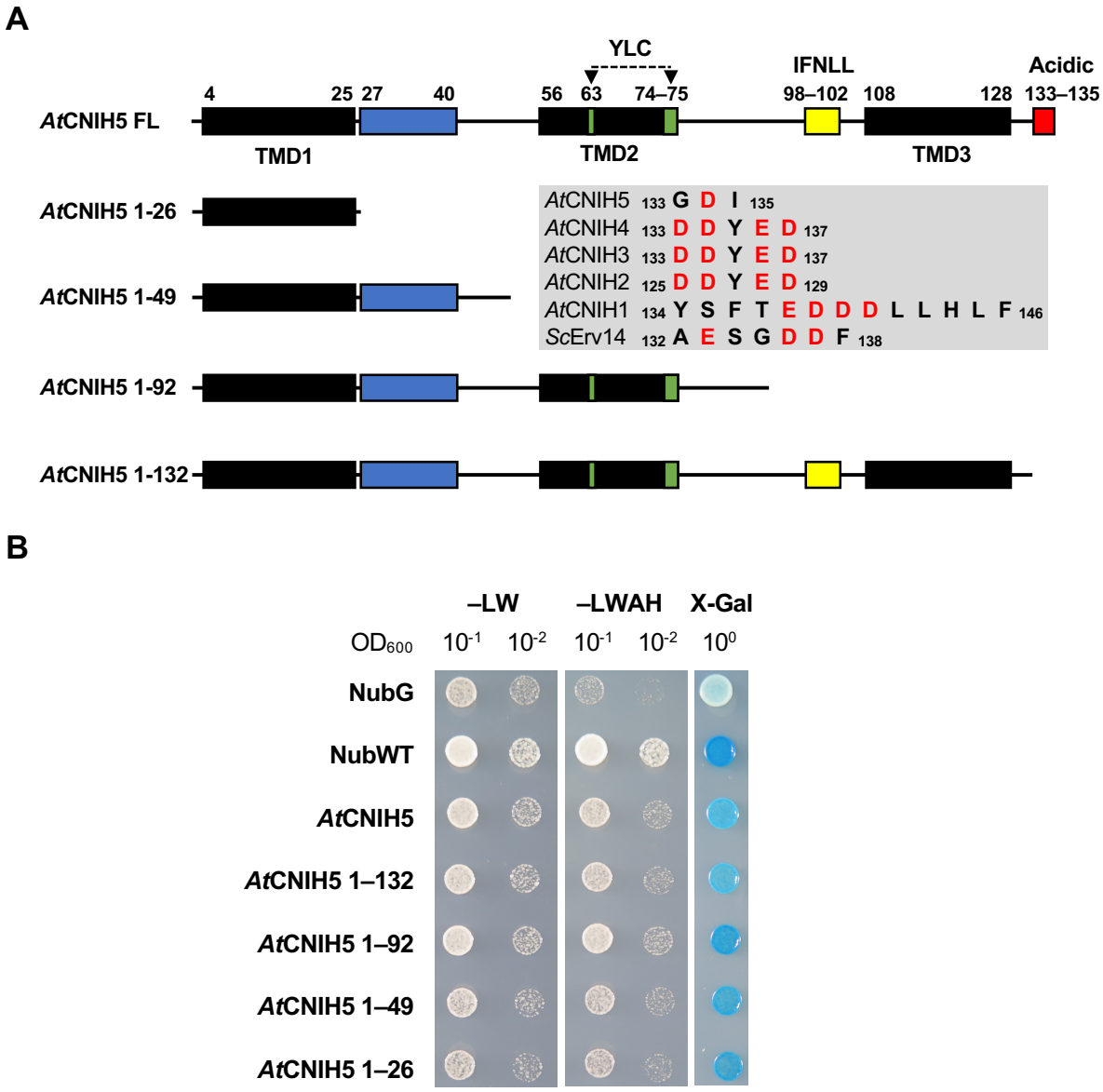

Figure 7. Analysis of the interaction of *At*PHT1;1 and the truncated *At*CNIH5 variants by the yeast split ubiquitin assay.

(A) Schematic diagram of full-length (FL) and truncated *At*CNIH5 variants. The length of the truncated variants are indicated by the number of residues. The transmembrane domains and the putative cornichon, YLC, IFNLL, and acidic motifs are shown. The black box, the transmembrane domain (TMD); the blue box, the cornichon motif; the green box, the YLC motif; the yellow box, the IFNLL motif. The red box, the acidic motif. The gray box shows the sequence alignment of the putative acidic motif of *Sc*Erv14 and *At*CNIHs. Noted that *At*CNIH5 has a shorter C-terminal tail carrying only one acidic residue D134.

(B) Co-expression of *At*PHT1;1-PLVCub with NubG-*At*CNIH5, NubG-*At*CNIH5 1–26, NubG-*At*CNIH5 1–49, NubG-*At*CNIH5 1–92, and NubG-*At*CNIH5 1–132. The co-expression of *At*PHT1;1-PLVCub with NubWT and NubG are used as positive and negative controls, respectively. Yeast transformants were grown on synthetic medium without leucine and tryptophan (–LW; the left panel) or on synthetic medium lacking leucine, tryptophan, adenine, and histidine with 500 μM methionine (–LWAH; middle panel) or on SC–LW containing 100 mg/L X-Gal (X-Gal; the right panel).

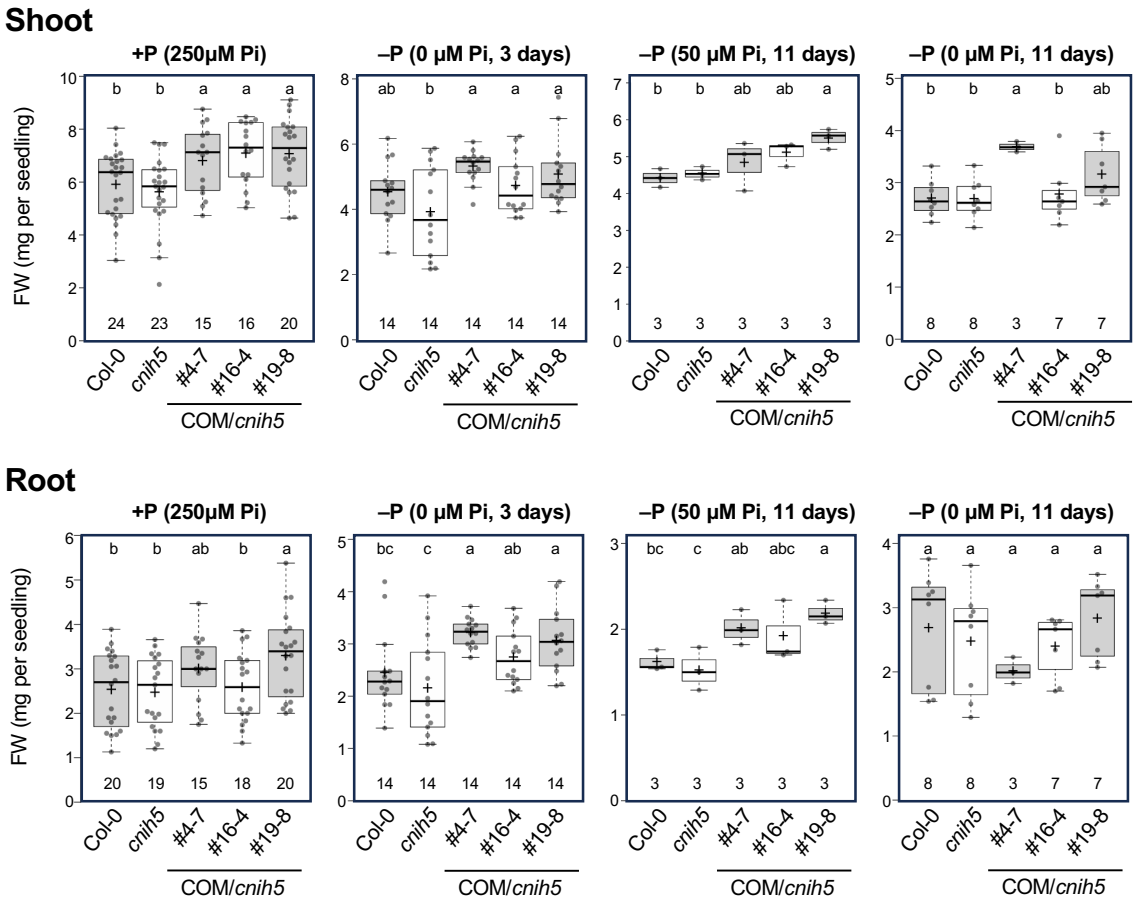

Figure 8. Increasing *in-situ At*CNIH5 expression/activity boosts plant growth.
The shoot and root fresh weight (FW) of *Arabidopsis* 11-day-old WT, *cnih5* and *AtCNIH5pro*: GFP-*AtCNIH5/cnih5* complementation (COM) lines under Pi-sufficient (+P, 250 μM KH_2PO_4), modest Pi-deficient (–P, 0 μM KH_2PO_4, three days of starvation or 50 μM KH_2PO_4, eleven days of starvation), and severe Pi-deficient (–P, 0 μM KH_2PO_4, eleven days of starvation) conditions. Data are visualized using BoxPlotR . Center lines show the medians; the central plus signs (+) show the means; box limits indicate the 25th and 75th percentiles; whiskers extend to the 5th and 95th percentiles, and data points are plotted as dots. Data significantly different from the other groups are indicated by different lowercase letters (n, pools of seedings from independent experiments; One-Way ANOVA, Duncan's test).

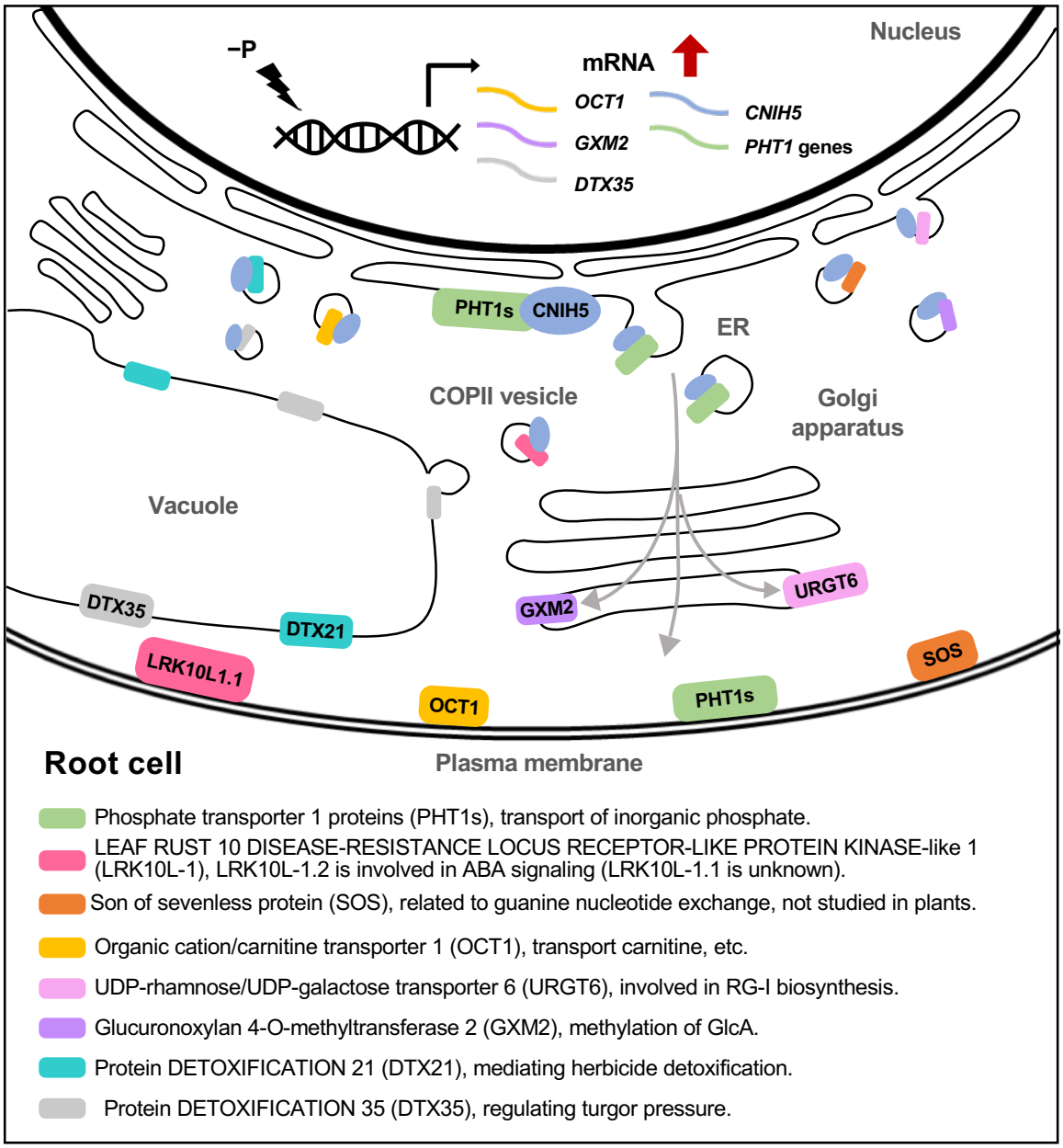

Figure 9. *At*CNIH5-mediated ER-to-Golgi transport of membrane proteins associated with Pi starvation responses in *Arabidopsis* root.

Under Pi starvation (−P), the transcripts of *CNIH5*, *PHT1* genes, *OCT1*, *GXM2*, and *DTX35* increase in *Arabidopsis* root cells . As an ER cargo receptor, CNIH5 assists the ER export of the newly synthesized PHT1s, LRK10L-1.1, SOS, OCT1, URGT6, GXM2, DTX21, and DTX35 and their loading into COPII vesicles, thus their corresponding subcellular destinations.

Table 1. List of the 31 downregulated microsomal transmembrane proteins in Pi-limited *cnih5* roots.
The normalized ratios compared the protein expression in Col-0_1, Col-0_2, *cnih5*_1 and *cnih5*_2 samples. The FDR adj. *p*-values were in the parentheses. The candidates highlighted in gray were selected for testing protein–protein interaction in this study. Subcellular localization is predicted or annotated by SUBA5, UniprotKB or experimental data.

AGI code	Accession	Gene name	*cnih5*_1/ Col-0_1	*cnih5*_2/ Col-0_1	*cnih5*_1/ Col-0_2	*cnih5*_2/ Col-0_2
		ER				
AT1G04220	Q5XEP9	3-ketoacyl-CoA synthase 2 (*AtKCS2*)	0.73 (0.57)	0.72 (0.66)	0.99 (0.99)	0.98 (1.00)
AT1G34130	Q9FX21	Dolichyl-diphosphooligosaccharide--protein glycosyltransferase subunit STT3B (*AtSTT3B*)	0.75 (0.53)	0.65 (0.30)	0.91 (0.91)	0.77 (0.38)
AT1G51740	P59277	Syntaxin-81 (*AtSYP81*)	1.18 (0.97)	0.73 (0.88)	0.94 (0.98)	0.58 (0.52)
AT3G23175	Q8GYI3	HR-like lesion-inducing protein-like protein	0.68 (0.23)	0.69 (0.46)	0.94 (0.97)	0.96 (0.99)
AT3G23190	Q9LTC9	HR-like lesion-inducing protein-like protein	0.94 (0.99)	0.63 (0.20)	0.92 (0.92)	0.62 (0.00)
AT3G48570	Q9SMP2	Protein transport protein Sec61 subunit gamma-3 (*AtSEC61G3*)	0.72 (0.30)	0.69 (0.42)	0.71 (0.02)	0.72 (0.12)
AT4G14420	O23298	HR-like lesion-inducing protein-like protein	0.76 (0.53)	0.61 (0.07)	0.81 (0.30)	0.64 (0.00)
At5G43760	Q9FG87	3-ketoacyl-CoA synthase 20 (*AtKCS20*)	1.03 (1.00)	0.60 (0.54)	1.23 (0.93)	0.72 (0.80)
		Golgi				
AT1G34020	Q9FDZ5	UDP-rhamnose/UDP-galactose transporter 6 (*AtURGT6*)	0.60 (0.49)	0.45 (0.18)	0.68 (0.69)	0.50 (0.27)
AT2G03480	Q3EC77	QUASIMODO2 LIKE 2 (*AtQUL2*)	0.78 (0.73)	0.64 (0.35)	0.87 (0.86)	0.68 (0.27)
AT2G40380	Q9SIY7	Prenylated Rab acceptor 1 (PRA1) family protein B2 (*AtPRA1B2*)	0.66 (0.26)	0.74 (0.72)	0.94 (0.97)	1.05 (0.99)
AT4G09990	Q9T0F7	Glucuronoxylan 4-O-methyltransferase 2 (*AtGXM2*)	0.71 (0.76)	0.73 (0.87)	0.58 (0.36)	0.60 (0.54)
AT4G30440	Q9M0B6	UDP-glucuronate 4-epimerase 1 (*AtGAE1*)	0.83 (0.93)	0.64 (0.58)	0.88 (0.93)	0.68 (0.38)
AT4G38270	Q0WQD2	Galacturonosyltransferase 3 (*AtGAUT3*)	0.87 (0.92)	0.62 (0.32)	0.95 (0.98)	0.69 (0.17)
At5G25100	Q9C5N2	Transmembrane 9 superfamily member 9 (*AtTMN9*)	0.73 (0.69)	0.81 (0.89)	0.70 (0.33)	0.78 (0.62)
		Vacuole				
AT1G33110	Q8W488	Protein DETOXIFICATION 21 (*AtDTX21*)	0.52 (0.00)	0.76 (0.77)	0.48 (0.00)	0.71 (0.40)
AT4G17340	Q41975	Tonoplast intrinsic protein 2;2 (*AtTIP2-2*)	0.88 (0.95)	0.91 (0.97)	0.65 (0.34)	0.64 (0.40)
AT4G25640	F4JTB3	Protein DETOXIFICATION 35 (*AtDTX35*)	0.86 (0.89)	0.66 (0.31)	0.89 (0.83)	0.68 (0.02)
At5G46090	Q9FNL3	DUF679 domain membrane protein 6 (*AtDMP6*)	0.74 (0.39)	0.64 (0.22)	0.86 (0.65)	0.74 (0.17)
		PM				
AT1G05570	Q9AUE0	Callose synthase 1 (*AtCALS1*)	0.74 (0.60)	0.73 (0.66)	0.82 (0.72)	0.80 (0.75)
AT1G17620	Q9LNP3	Late embryogenesis abundant (LEA) hydroxyproline-rich glycoprotein family	0.73 (0.54)	0.61 (0.23)	0.93 (0.96)	0.78 (0.68)
AT1G18390	P0C5E2	LEAF RUST 10 DISEASE-RESISTANCE LOCUS RECEPTOR-LIKE PROTEIN KINASE-like 1.2 (*AtLRK10L-1.2*)	0.74 (0.35)	0.72 (0.53)	0.75 (0.09)	0.73 (0.15)
AT1G26650	Q9LQY7	Son of sevenless protein (*AtSOS*)	0.61 (0.22)	0.70 (0.70)	0.61 (0.09)	0.70 (0.27)
AT1G73220	Q9CAT6	Organic cation/carnitine transporter 1 (*AtOCT1*)	0.89 (0.93)	0.86 (0.93)	0.73 (0.04)	0.69 (0.05)
AT2G27140	Q9ZVC6	HSP20-like chaperones superfamily protein	1.00 (0.99)	0.61 (0.13)	1.11 (0.87)	0.65 (0.01)
AT3G02600	Q8LFD1	Lipid phosphate phosphatase 3 (*AtLPP3*)	0.89 (0.92)	0.62 (0.16)	0.97 (0.98)	0.68 (0.02)
AT3G61270	Q9M2D7	Glycosyltransferase (*AtT20K12.170*)	0.84 (0.89)	0.67 (0.46)	0.80 (0.58)	0.64 (0.13)
AT4G01830	Q9SYI3	ATP binding cassette (ABC) transporter B family member 5 (*AtABCB5*)	0.75 (0.79)	0.68 (0.71)	0.99 (1.00)	1.03 (1.00)
At5G20970	F4K6X6	HSP20-like chaperones superfamily protein	0.85 (0.86)	0.51 (0.00)	1.10 (0.89)	0.66 (0.01)
At5G43350	Q8VYM2	Inorganic phosphate transporter 1;1 (*AtPHT1;1*)	0.63 (0.41)	0.54 (0.28)	0.65 (0.31)	0.56 (0.22)
At5G43360	O48639	Inorganic phosphate transporter 1;3 (*AtPHT1;3*)	0.58 (0.00)	0.65 (0.24)	0.56 (0.00)	0.74 (0.14)

Table 2. Summary of *At*PHT1s and *At*PHF1 expression in Pi-limited WT and *cnih5* roots.
The normalized ratios compared the protein expression in Col-0_1, Col-0_2, *cnih5*_1 and *cnih5*_2 samples. The FDR adj. *p*-values were in the parentheses.

Accession	Gene name	AGI code	Coverage [%]	Unique peptides	*cnih5*_1 /Col-0_1	*cnih5*_2 /Col-0_1	*cnih5*_1 /Col-0_2	*cnih5*_2 /Col-0_2
Q8GYE0	*AtPHF1*	AT3G52190	40	13	1.45 (0.05)	1.37 (0.36)	1.16 (0.48)	1.14 (0.62)
Q8VYM2	*AtPHT1;1*	AT5G43350	38	2	0.63 (0.41)	0.54 (0.28)	0.65 (0.31)	0.56 (0.22)
Q96243	*AtPHT1;2*	AT5G43370	30	1	0.61 (0.05)	0.97 (1.00)	0.78 (0.47)	1.24 (0.67)
O48639	*AtPHT1;3*	AT5G43360	10	2	0.58 (0.00)	0.65 (0.24)	0.56 (0.00)	0.74 (0.14)
Q96303	*AtPHT1;4*	AT2G38940	12	6	0.77 (0.40)	0.86 (0.89)	0.79 (0.06)	0.70 (0.00)
Q8GYF4	*AtPHT1;5*	AT2G32830	6	2	0.82 (0.78)	0.73 (0.58)	0.90 (0.87)	0.80 (0.42)
Q9S735	*AtPHT1;9*	AT1G76430	5	2	1.00 (0.99)	1.79 (0.20)	1.27 (0.79)	2.88 (0.00)

Coverage [%]: The percentage of the protein sequences covered by identified peptides.

Unique peptides: The total number of distinct peptide sequences unique to the protein group.